Anomalous diffusion and Lévy walks in optical lattices

S. Marksteiner, K. Ellinger, and P. Zoller
Institute for Theoretical Physics, University of Innsbruck, Technikerstrasse 25, A-6020 Innsbruck, Austria
(Received 12 October 1995)

We study theoretically the spatial diffusion (transport) of two-level atoms in one- and two-dimensional optical molasses derived from counterpropagating laser beams. We use both quantum Monte Carlo and semiclassical methods to study the microscopic characteristics of the atomic motion and their effect on the macroscopic behavior of the spatial distribution. We find that there exists a certain critical depth of the optical potential below which the atomic trajectories show Lévy flights in space that last on a definite time scale (Lévy walks). This behavior leads to a transition from Gaussian spatial diffusion to anomalous diffusion while crossing this critical potential depth. We show that only atoms with very high momentum are responsible for these Lévy walks. This observation allows us to predict the critical parameters via a semiclassical Fokker-Planck equation approach.

PACS number(s): 42.50.Vk, 32.80.Pj

I. INTRODUCTION

Laser cooling of atoms can be achieved in optical molasses, where counterpropagating laser beams provide a damping mechanism, and lead to the formation of optical potentials corresponding to a spatially varying ac Stark shift of the atomic ground states [1,2]. The generic model of laser cooling is an angular momentum $J_g=\frac{1}{2}$ to $J_e=\frac{3}{2}$ transition driven by two counterpropagating linearly polarized lasers with orthogonal polarizations. For red laser detuning and low laser intensities the optical potentials corresponding to the two ground states form an alternating pattern of optical bipotentials $U_{m_g=\pm 1/2}(z)$. Spontaneous emission causes transitions between these potentials via optical pumping processes. In the semiclassical picture of Sisyphus cooling [3] one considers an atom moving on one of these potential curves, and for red laser detuning transitions to the other potential then occur preferentially from the tops of $U_{-1/2}(z)$ down to the valleys of $U_{+1/2}(z)$, so that on the average the atomic motion is damped. Quantum mechanically, laser cooling can be understood as optical pumping between the quantized energy levels (band structure in the periodic optical potential) [4]. The temperatures achieved in experiments correspond to the accumulation of atoms in the few lowest vibrational energy levels. Transitions between the vibrational states will manifest themselves as sidebands (Raman transitions due to optical pumping) in atomic absorption and emission spectra [5]. From the physical picture derived from this model it is clear that laser cooling is intrinsically connected with a random walk of the atom (transport and spatial diffusion) in the optical lattice. It is the purpose of this paper to present a theoretical study of this spatial diffusion process. The final goal is to give a *physical* explanation for the divergence of the spatial diffusion constant of a $\frac{1}{2}\rightarrow\frac{3}{2}$ atom in a lin$\perp$lin laser configuration as predicted in a semiclassical Fokker-Planck treatment by Hodapp *et al.* [6].

We will start our discussion below with a fully quantum-mechanical investigation of spatial diffusion of $\frac{1}{2}\rightarrow\frac{3}{2}$ atoms in a one-dimensional (1D) optical molasses formed by a lin$\perp$lin laser configuration (see Ref. [7] and references cited therein). The basis is the quantum Monte Carlo wave function simulation with ''spatially localizing quantum jumps'' as developed by Holland *et al.* [8]. This simulation corresponds to a *spatially resolved* photodetection of the spontaneously emitted photon, and can be visualized as an ''experiment with a Heisenberg microscope'' where the atom moving in the optical molasses is ''continuously monitored through a lens'' and the locus of spontaneously emitted photons is simulated. Each ''observation'' of a photon thus localizes the atom with the accuracy of a laser wavelength, and in this sense we can give an operational definition to a quantum trajectory of an atom moving in space. It can be shown [8] that an averaging over many realizations is equivalent to a solution of the standard master equation of laser cooling [1,2]. The scheme has the significant numerical advantage that each occurrence of a quantum jump localizes the atoms in space and we can allocate a relatively small dynamic grid for the atomic wave function to ''follow'' the motion of the atom in space. A typical example for one of these simulated trajectories is depicted in Fig. 1. The upper part of Fig. 1 shows the expectation value for the position of the Monte Carlo wave function as a function of time. The lower plot shows the total energy, i.e., kinetic plus potential, on the same time scale. We see that the trajectory consists of two very different types of motion. First, there are the more or less horizontal lines, where the atom is trapped in the wells of the optical lattice, having an energy below the potential barrier (indicated by the dashed line in Fig. 1) between adjacent minima. The atom stays more or less in this well, occasionally shifting to the neighboring ones. But at some stage energy fluctuations due to spontaneous emissions allow the atom to accumulate enough energy to be sufficiently high above the barrier [9]. It then takes off on a flight that can reach over many wavelengths (indicated by the shaded regions in Fig. 1) until it is eventually trapped again.

This behavior is reminiscent of random walk processes with long flights, which have been studied in the mathematical literature under the name of Lévy flights [10,11]. The defining property of Lévy flights is that the jump distance for each consecutive step is drawn from a distribution whose variance diverges. In the context of laser cooling this type of

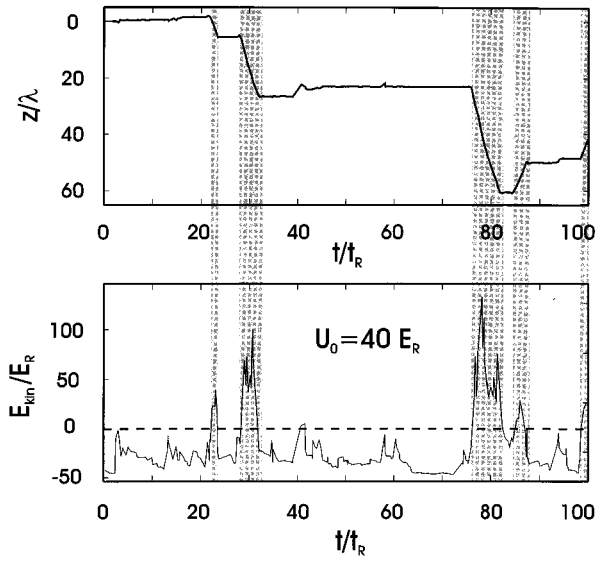

FIG. 1. A ''typical'' trajectory of an atom in a 1D lin⊥lin optical lattice with a potential depth of $U_0=40E_R$. The upper plot shows the expectation value of the position for the stochastic wave function as a function of time (in units of $t_R=E_R/\hbar$). The lower plot shows the corresponding total energy of the atom. The shaded areas correspond to a motion of the atom above the barrier between adjacent potential minima where the atom travels over many wavelengths. The regions left white correspond to below-barrier motion where the atom is trapped in the wells of the optical lattice.

behavior has been found in laser configurations that give rise to velocity-selective dark states [12]. In this case the Lévy character of the random process results from long waiting times (when the atom is trapped in a momentum state close to the dark state).

A characteristic feature of Lévy-type random processes is that the distribution of the total distance traveled after n steps does not approach a Gaussian in the limit $n\rightarrow\infty$, i.e., the central limit theorem [10] is not applicable. Instead the limit distribution is given by a Lévy law that possesses slowly decaying wings [10]. As a consequence the asymptotic dependence of the width of this distribution on the step number n is given by

$$\Delta z(n)^2=\langle z^2\rangle_n-\langle z\rangle_n^2\sim n^\gamma \quad \text{with} \quad \gamma\neq 1, \tag{1}$$

where $\langle z\rangle_n$ and $\langle z^2\rangle_n$ denote the expectation value for the total distance and the total squared distances traveled after n steps of the random walk, respectively. Another remarkable property is that the underlying microscopic process (i.e., the trajectory of the random walk) shows longer and longer ''flights'' the longer we observe the system (hence the name Lévy flights) and thus has a self-similar (fractal) nature [11]. In other words, if we look at a trajectory like the one in Fig. 1 we will find that the total distance that the particle traveled is dominated by a single flight, no matter on what time scale we look at the trajectory.

As has been emphasized by Shlesinger, Zaslavsky, and Klafter [11], the elegant mathematics of Lévy flights is not directly applicable to the kinetic description of real *dynamical* processes. In the case of Lévy flights the time aspect of the flight (i.e., the time it takes to complete it) does not enter. If this dynamical aspect of the flights is included these processes are named Lévy *walks* according to Ref. [11].

In generalizing (1) the spatial diffusion of *dynamical* quantum systems can be characterized by the time evolution of the squared width [11]

$$\Delta\hat{z}(t)^2=\langle\hat{z}^2\rangle_t-\langle\hat{z}^2\rangle_t, \tag{2}$$

where $\langle A\rangle_t$ denotes—as usual—the quantum-mechanical expectation value for an arbitrary operator A,

$$\begin{aligned}\langle A\rangle_t&\equiv \mathrm{tr}_{S+B}A|\Psi(t)\rangle\langle\Psi(t)|\\&=\mathrm{tr}_{S+B}A(t)|\Psi(0)\rangle\langle\Psi(0)|\end{aligned} \tag{3}$$

in the Schrödinger and Heisenberg pictures, respectively. Since we are dealing here with an ''open system,'' i.e., a system (atom) that is coupled to a ''bath'' (quantized electromagnetic field), we must trace over both system and bath.

Many physical systems show a time evolution of the spatial distribution converging to a Gaussian,

$$W(\boldsymbol{x},t)\sim\frac{1}{\sqrt[3]{4\pi D_z t}}\exp[-\boldsymbol{x}^2/4D_z t], \tag{4}$$

and thus are characterized in the above sense by $\Delta\hat{z}(t)^2\sim 2D_z t$. Throughout this paper we will denote asymptotic expansions with a tilde. The long-time behavior of this type of diffusion is solely described by the *spatial diffusion constant* D_z, which is defined by [13]

$$D_z=\lim_{t\rightarrow\infty}\frac{1}{2}\frac{d}{dt}\Delta\hat{z}(t)^2. \tag{5}$$

A deviation from this linear behavior, i.e., $\Delta\hat{z}(t)^2\sim t^\gamma$ ($\gamma\neq 1$), defines anomalous diffusion [11]. In our context the existence of a spatial diffusion constant is best discussed by reexpressing (5) in terms of the (symmetrized) momentum correlation function (see Sec. II C for details)

$$D_z=\lim_{t\rightarrow\infty}\frac{1}{M^2}\int_0^t d\tau\langle\hat{p}(\tau),\hat{p}(t)\rangle_{\mathrm{sym}}. \tag{6}$$

We will show that in the case of 1D lin⊥lin optical molasses the momentum correlation function for a $\frac{1}{2}$ to $\frac{3}{2}$ transition decays with the characteristic law

$$\langle\hat{p}(t),\hat{p}(t+\tau)\rangle_{\mathrm{sym}}\propto\tau^{-\mu}, \tag{7}$$

where the critical parameter μ is related to the depth of the optical potential U_0 by

$$\mu=\frac{5}{123}\frac{U_0}{E_R}-\frac{3}{2}, \tag{8}$$

with recoil energy $E_R=\hbar^2k^2/2M$. For $\mu>1$ the integral (6) converges and the diffusion constant (5) exists; below $\mu=1$—corresponding to a critical potential depth $U_0^{\mathrm{crit}}=61.5E_R$—there is a transition to anomalous diffusion.

Lévy walks are associated with atomic motion in the optical molasses far above the potential barrier. In this energy

range a semiclassical description in terms of a Fokker-Planck equation (FPE) is appropriate and provides the basis for the analytical description of these phenomena. Note, however, that the FPE cannot be employed to describe the below barrier motion (the localization regime). Only for the special case of a $J_g=\frac{1}{2}\rightarrow J_e=\frac{3}{2}$ transition can one formulate a semiclassical bipotential model (which includes localization) [14] since in this case no Zeeman coherences exist between the ground states.

A final question studied in this paper is the existence of Lévy walks in 2D optical lattices. We will present results for two laser configurations [15–17] based on FPE treatment for a $\frac{1}{2}$ to $\frac{3}{2}$ atom that is verified by a semiclassical bipotential simulation.

II. QUANTUM MECHANICAL TREATMENT OF SPATIAL DIFFUSION IN ONE DIMENSION

In this section we will investigate the spatial diffusion of atoms in an optical molasses in a fully quantum-mechanical framework. Due to the complexity of the underlying equations of motion we will restrict this treatment to one-dimensional laser configurations.

After a brief review of the basic equations of 1D laser cooling we will solve these equations with the initial condition that the atom is localized to a single well in the optical potential. It is in principle possible to calculate the time evolution of this system by using the standard quantum Monte Carlo (QMC) method as described in Refs. [7,18]. The key feature of this simulation scheme is that the emission *direction* (and polarization) of the photon is measured. We will therefore refer to the measurement that is simulated by this simulation method as *angle resolved photon detection*. By emitting a photon in a certain direction the atom receives a momentum kick in the opposite direction. Formally, this kick is transferred to the atom by applying the operator

$$K_{\sigma u}(\hat{z})=\sqrt{N_\sigma(u)}B_\sigma(\hat{z})e^{-iu\hat{z}} \tag{9}$$

(see Sec. II A for details) to the wave function. Unfortunately, this simulation method leads to an unlimited spatial spreading of the stochastic wave function in the course of its evolution since the application of the kick operators (9) does not reduce the spatial coherence length of the atomic wave function. The angle resolved photon detection is therefore not able to reduce the unavoidable spreading of the stochastic wave function during its coherent propagation (i.e., in between the quantum jumps). Hence, storing the (discretized) wave function on a computer requires an ever growing memory grid, which at some point will either lead to memory problems or will render the propagation algorithm inefficient [19].

It is therefore desirable to avoid this spreading and we have shown in Ref. [8] that this can be achieved by simulating a measurement of the emission locus of the spontaneous photon instead of the emission direction. In Sec. II B we will briefly review this method and utilize it in order to study the time evolution of an initially well localized cloud of noninteracting atoms.

In Sec. II C we will use an alternative, indirect approach that makes use of a relation between the spatial diffusion constant and the momentum correlation function. For the calculation of these correlation functions it is advantageous to use the standard QMC technique again (cf. Appendix A).

A. Basic equations for one-dimensional laser cooling

In this section we summarize and review the basic equations of one-dimensional laser cooling in order to identify the physical parameters in our model and to establish our notation. For details we refer to Refs. [4,7,20]. In our 1D model we consider a two-level atom with a Zeeman substructure corresponding to an angular momentum J_g to J_e transition in a laser configuration consisting of two counterpropagating light beams with linear and orthogonal polarization (lin$\perp$lin). In this configuration the positive frequency part of the electric field can be written as

$$\boldsymbol{E}^+_{\rm cl}(z,t)=\mathscr{E}\sqrt{2}[\cos(kz)\boldsymbol{e}_+ +\sin(kz)\boldsymbol{e}_-]e^{-i\omega_L t}. \tag{10}$$

Here $\mathscr{E}$ is the light amplitude, ω_L and k denote the laser frequency and wave vector, z is the coordinate along the light propagation axis (which is also the quantization axis for the atom), and $\boldsymbol{e}_\pm=\mp(1/\sqrt{2})(\hat{\mathbf{x}}\pm i\hat{\mathbf{y}})$ are spherical unit vectors.

We are interested in laser intensities well below saturation $s_0\ll 1$, which give rise to the lowest temperatures corresponding to the largest ground-state population. The saturation parameter is defined as $s_0=\frac{1}{2}\Omega^2/(\Delta^2+\frac{1}{4}\Gamma^2)$, with $\Omega=2\mathscr{E}d/\hbar$ the Rabi frequency, d the dipole matrix element on the outermost Zeeman transition $M_g=J_g\rightarrow M_e=J_e$, Γ the spontaneous decay rate, and $\Delta=\omega_L-\omega_{eg}$ the laser detuning. Elimination of the excited-state manifold leads to the generalized optical Bloch equation (GOBE) for the ground-state density matrix $\rho(t)$, [7],

$$\dot{\rho}=-\frac{i}{\hbar}(h_{\rm eff}\rho-\rho h^\dagger_{\rm eff})+2\gamma_0\sum_{\sigma=0,\pm1}\int_{-k}^{+k}duK_{\sigma u}(\hat{z})\rho K^\dagger_{\sigma u}(\hat{z}), \tag{11}$$

with the momentum kick (or angle resolved photon detection [8]) jump operators

$$K_{\sigma u}(\hat{z})=\sqrt{N_\sigma(u)}B_\sigma(\hat{z})e^{-iu\hat{z}}, \tag{12}$$

and the non-Hermitian effective Hamiltonian

$$h_{\rm eff}=\frac{\hat{p}^2}{2M}+\frac{\hbar s_0}{2}\left(\Delta-i\frac{\Gamma}{2}\right)\mathscr{D}(\hat{z})\mathscr{D}^\dagger(\hat{z}). \tag{13}$$

The dipole operator $\mathscr{D}(\hat{z})$ is given by

$$\mathscr{D}(\hat{z})=\sum_{\sigma=0,\pm1}(-1)^\sigma A_\sigma\epsilon^*_{-\sigma}(\hat{z}), \tag{14}$$

where

$$A_\sigma=\sum_{M_e,M_g}|J_gM_g\rangle\langle J_gM_g;1\sigma|J_eM_e\rangle\langle J_eM_e| \tag{15}$$

denotes the atomic lowering operator involving the emission of a photon of polarization σ and the space-dependent coefficients $\epsilon_\sigma(z)$ of the polarization vectors relate to the electric field via

$$\mathbf{E}_{\mathrm{cl}}^{(+)}(z,t)=\mathscr{E}\sum_{\sigma=0,\pm1}\boldsymbol{\epsilon}_\sigma(z)\mathbf{e}_\sigma^{*}e^{-i\omega_L t}\left(\sum_\sigma|\boldsymbol{\epsilon}_\sigma(z)|^2=1\right). \quad (16)$$

The first two terms on the right-hand side of Eq. (11) correspond to a time evolution due to the Hamiltonian h_{eff}, while the last term describes the return of the atomic electron to the ground state by optical pumping.

The Hermitian part of h_{eff} governs the coherent 1D motion of a particle in the periodic optical potential

$$U(\hat{z})=-\frac{s_0\hbar\Delta}{2}\mathscr{D}(\hat{z})\mathscr{D}^{\dagger}(\hat{z}), \quad (17)$$

as given by the ac Stark shift of the various Zeeman sublevels. In the following, we will refer to $U_0=-\frac{1}{2}s_0\hbar\Delta$ as the potential depth, which we usually give in units of the recoil energy $E_R=\hbar\omega_R=\hbar^2k^2/2M$. Since our laser configuration involves no π-polarized light component, this coherent evolution couples only states that are connected by a σ_+-σ_- Raman transition, i.e., states whose M_g differ by two. The anti-Hermitian part in (13) leads to a damping due to optical pumping with $\gamma_0=\frac{1}{4}s_0\Gamma$ the optical pumping rate between the ground-state levels. The operators $B_\sigma(\hat{z})=A_\sigma\mathscr{D}^{\dagger}(\hat{z})$ in the jump operators (12) describe a Raman transition, corresponding to absorption of a laser photon ($\mathscr{D}^{\dagger}$) followed by spontaneous emission of a photon (A_σ) with light polarization $\sigma=0,\pm1$. The angular distributions of spontaneously emitted photons with polarization σ are given by

$$N_0(u)=\frac{3}{4k}[1-(u/k)^2],$$

$$N_{\pm1}(u)=\frac{3}{8k}[1+(u/k)^2]. \quad (18)$$

As is shown in Ref. [18], a solution of (11) can be calculated by simulating stochastic trajectories that correspond to a coherent evolution of the atomic wave function, which is interrupted at random times by the emission of spontaneous photons. The density matrix at a certain time is then recovered by averaging over many of these trajectories. This approach is called quantum Monte Carlo wave-function simulations. A pictorial view of this method is to consider the bath of quantized electromagnetic field modes as being used as a meter to continuously monitor the atom. Each time a photon is detected in the bath we can calculate the back action that this emission has had on the atom. By doing this the evolution of the density matrix $\rho(t)$ in the GOBE is replaced by an average over pure-state trajectories that correspond to stochastically chosen photon emission times and decay channels (for example, emission direction and polarization of the photon). The numerical advantage of dealing with wave functions instead of density matrices is evident since the dimension of a wave function is proportional to the number N of basis states (in our case the number of points of a discretized spatial grid), whereas the density matrix scales as N^2 (see also the discussion in Ref. [7]).

B. Direct simulation of atomic motion using localizing quantum jumps

As already mentioned the key idea behind the method of localizing quantum jumps is the simulation of a measurement process for the emitted photons that gives us information on the position of the atom. This can be visualized as follows: instead of detecting the emission direction as in the standard QMC approach we ''look at the atom via an imaging system'' such as, e.g., a microscope lens and thereby detect where the spontaneous photon came from. The mathematical implementation of a measurement process that can be interpreted in this way is given by the following unitary transformation of the angle resolved jump operators [8]:

$$J_{\sigma m}(\hat{z})=\int_{-k}^{k}du\,\frac{e^{imu\lambda/2}}{\sqrt{2k}}K_{\sigma u}(\hat{z})\,(m=0,\pm1,\pm2,\ldots), \quad (19)$$

where the discrete index m corresponds to the detection position $z=m\lambda/2$ of the photon. From (19) and (12) we readily see that the spatial dependence of the jump operators $J_{\sigma m}(\hat{z})$ is given by the product of the Raman transition operators $B_\sigma(\hat{z})$ (which are periodic with period λ) and the Fourier transform of the angular distribution functions for spontaneous emission $N_\sigma(u)$. It is easy to check by explicitly calculating these Fourier transforms that the latter factor is similar to a $\sin(kz)/z$ function. The effect of applying the new jump operators $J_{\sigma m}(\hat{z})$ to a wave function is thus a reduction of the coherence length (i.e., the spatial width of the wave packet) to something on the order of the wavelength of the emitted photon (in compliance with the Heisenberg uncertainty principle). This results in the localization of the atom around the detection locus of the emitted photon. Another important property of the jump operators $J_{\sigma m}(\hat{z})$ is that they can be generated from a single one, say $J_{\sigma0}(\hat{z})$, by the translation

$$J_{\sigma m}(\hat{z})=J_{\sigma0}\left(\hat{z}-\frac{m\lambda}{2}\right). \quad (20)$$

By inverting Eq. (19),

$$K_{\sigma u}(\hat{z})=\sum_{m=0,\pm1,\pm2,\ldots}\frac{e^{-imu\lambda/2}}{\sqrt{2k}}J_{\sigma m}(\hat{z}), \quad (21)$$

and inserting it into (11) we get the transformed GOBE,

$$\dot{\rho}=-\frac{i}{\hbar}(h_{\mathrm{eff}}\rho-\rho h_{\mathrm{eff}}^{\dagger})+2\gamma_0\sum_{\sigma=0,\pm1}\sum_{m=0,\pm1,\ldots}J_{\sigma m}(\hat{z})\rho J_{\sigma m}^{\dagger}(\hat{z}). \quad (22)$$

Note that the physical content of the GOBE is of course not altered by this transformation. The conclusions drawn from this representation are therefore necessarily identical to the ones derived in Eq. (11). However, this new form leads to a simulation scheme for the problem at hand that is much more efficient than the angle resolved detection approach.

The procedure for calculating the trajectory corresponding to the simulation of a certain measurement record

$(\sigma_1 m_1, \sigma_2 m_2, \sigma_3 m_3, \ldots)$ for the polarization and emission loci of consecutive spontaneous photons and the subsequent averaging over many different measurement records can be summarized as follows.

(i) Initial condition. Any initial atomic density matrix $\rho(t=0)$ can be decomposed into a sum of projectors onto pure states, i.e., $\rho(t=0)=\Sigma_\lambda p_\lambda |\Phi_\lambda\rangle\langle\Phi_\lambda|$. We choose one of the pure states $|\Phi_\lambda\rangle$ as the initial condition for our stochastic trajectory according to the distribution p_λ. For the simulations in this subsection we start by definition with the atom in a pure state $\rho(t=0)=|\Phi_0\rangle\langle\Phi_0|$, where $|\Phi_0\rangle$ corresponds to an atomic wave function that is localized to a single quantum well in the optical potential.

(ii) Propagation. We propagate the wave function $|\Phi(t)\rangle$ according to the effective Schrödinger equation

$$i\hbar \frac{d}{dt}|\Phi(t)\rangle = h_{\text{eff}}|\Phi(t)\rangle. \tag{23}$$

This is a multicomponent Schrödinger equation that does not preserve the norm due to the anti-Hermitian part of h_{eff}. Note that this coherent propagation is not affected by the transformation (19).

In order to determine the time t^- for the next quantum jump we draw a uniform random number $r \in [0,1]$ and propagate $|\Phi(t)\rangle$ until the squared norm $\|\Phi(t^-)\|^2$ drops below this random number.

(iii) Quantum jump. As soon as we reach the time for the next quantum jump we have to choose a decay channel for the spontaneous photon. In the case of the localizing quantum jumps this amounts to choosing the polarization σ and emission locus $m\lambda/2$ according to the distribution

$$p(\sigma,m)=\tilde{c}\|J_{\sigma m}(\hat{z})|\Phi(t^-)\rangle\|^2, \tag{24}$$

where $\tilde{c}$ is some normalization constant. The wave function after the jump $|\Phi(t^+)\rangle$ is then given by

$$|\Phi(t^+)\rangle = \frac{J_{\sigma m}(\hat{z})|\Phi(t^-)\rangle}{\|J_{\sigma m}(\hat{z})|\Phi(t^-)\rangle\|}. \tag{25}$$

(iv) Averaging. After the jump we proceed with step (ii) and repeat the procedure until we reach the final propagation time t. We then use the resulting wave function $|\Phi(t)\rangle$ in order to improve the expectation value

$$\rho(t)=\left\langle\!\!\left\langle \frac{|\Phi(t)\rangle\langle\Phi(t)|}{\|\Phi(t)\|^2} \right\rangle\!\!\right\rangle. \tag{26}$$

Finally, we repeat the whole procedure starting with (i) until the prediction for $\rho(t)$ is sufficiently converged.

We already mentioned that every time we apply one of the new jump operators to the atom we collapse its wave function to the detection location of the spontaneous photon with a width corresponding to the wavelength of the photon. It is apparent that the repeated application of localizing jump operators enables us to store the wave function on a fixed-size spatial grid that we allocate dynamically to follow the atom [19].

We have used this approach in order to simulate the time evolution of an initially well localized atom in a 1D lin⊥lin optical molasses. The basic features of the trajectories as illustrated in Fig. 1 have already been discussed in the Introduction.

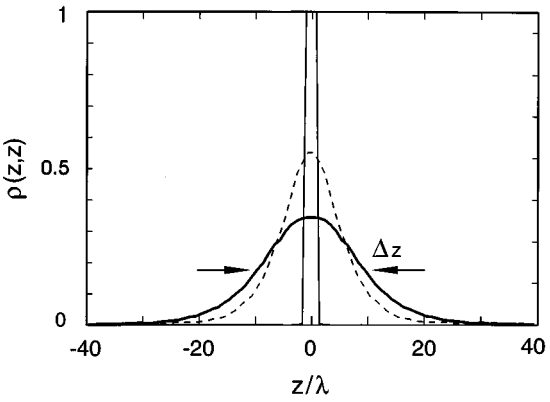

FIG. 2. Spatial distribution for $U_0=200E_R$ and $\gamma_0=3\omega_R$ at times $t=0$, $500\omega_R^{-1}$, and $1000\omega_R^{-1}$. The initial condition corresponds to an atom confined to a single well in the optical potentials. The arrows indicate the FWHM used for the calculation of the spatial diffusion constant.

By averaging over many of these trajectories (usually several hundred thousands) we recover the smooth spreading of the atomic density matrix as depicted in Fig. 2. Following the experimental procedure in Ref. [6], we calculate the spatial diffusion constant from the time derivative of the squared full width at half maximum Δ_{FWHM} of the spatial distribution. More precisely, this means that we calculate the evolution of the diagonal of the atomic density matrix $\langle z|\rho(t)|z\rangle$ (usually up to $t=1000\omega_R^{-1}$) and plot the squared FWHM as a function of time (cf. Fig. 3). This function converges in the case of a Gaussian diffusion after a certain initial transient (that depends critically on the system parameters) to a linear behavior and we can calculate the spatial diffusion constant from the slope of the linear asymptote:

$$D_z=\frac{1}{16\ln 2}\lim_{t\to\infty}\frac{d\Delta_{\text{FWHM}}(t)^2}{dt}. \tag{27}$$

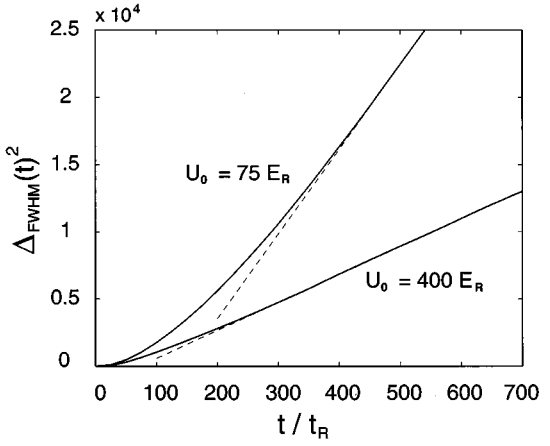

FIG. 3. Time dependence of $\Delta_{\text{FWHM}}(t)^2$ for a deep and a rather shallow optical potential depth. Note that $\Delta_{\text{FWHM}}(t)^2$ for the deep potential converges faster to a linear asymptote.

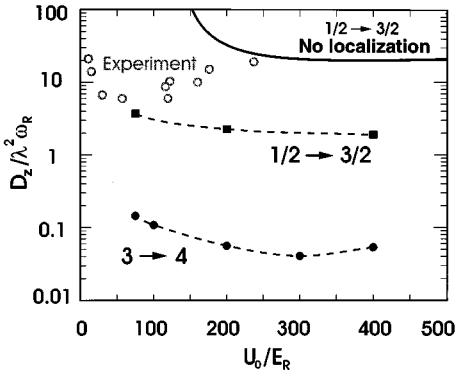

FIG. 4. Spatial diffusion constant versus potential depth. The solid line shows the result of the semiclassical Fokker-Planck theory of Ref. [6] ($\gamma_0 = 1.875\omega_R$). The filled circles and squares were calculated using a localizing quantum jump QMC method for a $J_g = 3 \rightarrow J_e = 4$ transition with $\gamma_0 = 3\omega_R$ and a $J_g = \frac{1}{2} \rightarrow J_e = \frac{3}{2}$ transition with $\gamma_0 = 1.875\omega_R$, respectively. A semiclassical bipotential simulation for $J_g = \frac{1}{2} \rightarrow J_e = \frac{3}{2}$ give results virtually identical to the full quantum treatment for this transition. The experimental points (open circles) were taken from Ref. [6] and correspond to the $F_g = 3$ to $F_g = 4$ transition of ^{85}Rb with for various γ_0's.

The behavior of the diffusion constant as a function of the potential depth U_0 is plotted in Fig. 4 for a $\frac{1}{2} \rightarrow \frac{3}{2}$ transition (solid squares) and a $3 \rightarrow 4$ transition (solid circles), and compared with a semiclassical Fokker-Planck theory for a $\frac{1}{2} \rightarrow \frac{3}{2}$ transition ignoring the localization of atoms in the optical potential wells [6] (solid line). A semiclassical bipotential simulation for $J_g = \frac{1}{2} \rightarrow J_e = \frac{3}{2}$ (which includes localization but is based on a semiclassical $\hbar k$ expansion) give results virtually identical to the full quantum treatment for $\frac{1}{2} \rightarrow \frac{3}{2}$.

For the sake of completeness we have also included experimental data for the $F_g = 3$ to $F_g = 4$ transition of ^{85}Rb [6] (light open circles). However, we would like to caution the reader not to compare them directly with the actual results depicted in Fig. 4. This is for two reasons: firstly, the experiment was set up in a six-beam 3D configuration whose light shift potentials cannot be compared directly with the 1D optical potentials used in this section (see also Sec. IV in which we discuss the effect on the potential when going to higher dimensions). Secondly and more important, phase fluctuations of the six laser beams lead to a temporal variation of the topography of the potential, producing potential hills where potential minima might have been a certain time before. A behavior like that would strongly reduce the localization of atoms in the moving potential minima and hence aid to the spatial diffusion. It is for this reason that a semiclassical approach that neglects localization [6] is appropriate to describe the atoms. In order to visualize this we have plotted the experimental data in Fig. 4 as light open circles.

The first apparent feature of Fig. 4 is that the predictions for the diffusion of the semiclassical Fokker-Planck treatment (which ignores localization and trapping of atoms in the wells of the optical potential) and the full quantum calculation for the same $\frac{1}{2} \rightarrow \frac{3}{2}$ transition deviate substantially. The presence of potential hills that separate the various potential wells necessitates that atoms must have a certain minimum kinetic energy in order to overcome the barrier between neighboring minima as they travel from one well to the other. Since atoms are very efficiently cooled in an optical molasses only a few percent of the particles have large enough energies to do so (cf. Ref. [8]). This localization effect is—by assumption—not included in the semiclassical FP approach used in Ref. [6] and hence particles with arbitrarily small momenta contribute to the spatial diffusion. We will give a simple extension of the theory used in Ref. [6] that is able to account for this effect in Sec. III [see Eq. (53)].

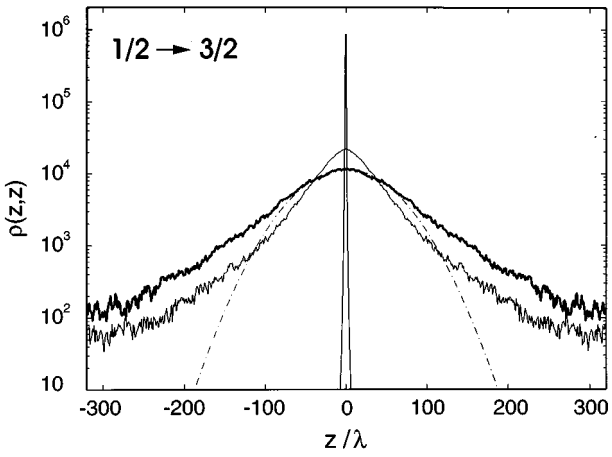

FIG. 5. Spatial distribution on a logarithmic scale for $U_0 = 75E_R$ and $\gamma_0 = 1.875\omega_R$ at times $t = 0$, $250\omega_R^{-1}$, and $500\omega_R^{-1}$. A Gaussian fit to the final distribution is indicated by the dash-dotted line.

A decrease of the spatial diffusion constant is found as we go to the $3 \rightarrow 4$ transition (corresponding, for example, to the Zeeman substructure of ^{85}Rb used in the experiment in Ref. [6]). In Ref. [8] we show that this can be explained by the fact that the number of atoms whose energies are larger than the barrier between adjacent adiabatic minima is five times lower for a $3 \rightarrow 4$ transition than for a $\frac{1}{2} \rightarrow \frac{3}{2}$ transition. In addition the light shift potential for $3 \rightarrow 4$ atoms is complicated by the existence of Raman coherences between different Zeeman sublevels. In order to travel to the neighboring well the atom has to adiabatically follow the avoided crossings in the adiabatic potentials [8]. Whether it is able to proceed to the neighboring well or is reflected back depends very much on how fast it approaches these crossings. This explains the strong suppression of spatial diffusion for this transition as compared to the $\frac{1}{2} \rightarrow \frac{3}{2}$ case.

In addition, according to Fig. 4 the QMC simulations do not show the divergence of the spatial diffusion constant in the FP theory at a potential depth of $135E_R$ [6], even though all curves exhibit a pronounced increase of the diffusion constant as U_0 decreases. However, we find that we run into severe convergence problems with the quantum Monte Carlo method when we lower U_0 below approximately $60E_R$. The lowest potential depth for the QMC curves in Fig. 4 is $U_0 = 75E_R$ and the corresponding time evolution of the spatial distribution ($\frac{1}{2} \rightarrow \frac{3}{2}$ transition) at various time steps is given in Fig. 5.

The numerical convergence problems mentioned result from the marked non-Gaussian wings that are clearly visible in the logarithmic plot. These wings become less pronounced

as we propagate the density matrix to larger times, but prevail for longer and longer as we lower the potential depth towards approximately $60E_R$ (cf. also Fig. 3). Slowly decaying parts of the spatial distribution are a typical feature of anomalous diffusion and are thus a strong indication that the character of the atomic motion undergoes a characteristic change as we reach the critical value of the potential depth.

It is the purpose of the subsequent sections to examine the physical mechanisms that lead to this change in behavior and to quantitatively predict its critical parameters.

C. Momentum correlation functions

In the Introduction we mentioned that the momentum correlation function is a powerful tool to investigate the problem of the divergence of the spatial diffusion constant for an atom in an optical molasses, as first encountered in Ref. [6]. In order to prove this let us first derive a relation between the spatial diffusion constant and the momentum correlation function.

As discussed in the Introduction, the spatial diffusion constant is defined by [13]

$$D_z = \lim_{t\to\infty} D_z(t), \tag{28}$$

with

$$2D_z(t) \equiv \frac{d}{dt}\Delta\hat{z}(t)^2. \tag{29}$$

Interchanging the differentiation and the trace and using the reflection symmetry of our problem (which leads to $\langle\hat{z}\rangle_t = \langle\hat{z}\rangle_0 = \text{const}$) we can rewrite this as

$$D_z(t) = \langle\hat{z}(t), \dot{\hat{z}}(t)\rangle_{\text{sym}}, \tag{30}$$

where we have used the definition for the symmetrized two-time expectation value

$$\langle A(t), B(\tau)\rangle_{\text{sym}} = \tfrac{1}{2}[\langle A(t)B(\tau)\rangle + \langle B(\tau)A(t)\rangle]. \tag{31}$$

The time derivative of the position operator is easy to evaluate since we are working in a dipole approximation and therefore the momentum operator only enters the Hamiltonian through the kinetic term $\hat{p}^2/2M$. We find $\dot{\hat{z}}(t) = \hat{p}(t)/M$ and therefore

$$\hat{z}(t) = \hat{z}(0) + \frac{1}{M}\int_0^t d\tau\, \hat{p}(\tau). \tag{32}$$

Inserting this into (29) we find

$$D_z(t) = \frac{1}{M}\langle\hat{z}(0), \hat{p}(t)\rangle_{\text{sym}} + \frac{1}{M^2}\int_0^t d\tau \langle\hat{p}(\tau), \hat{p}(t)\rangle_{\text{sym}}. \tag{33}$$

The first term on the right-hand side is the correlation of the momentum with the initial position and is thus a function that decays to zero for large times. The second term incorporates the correlation of the atomic momentum at time t with the momentum at earlier times τ and thus converges for large t to the stationary momentum correlation function

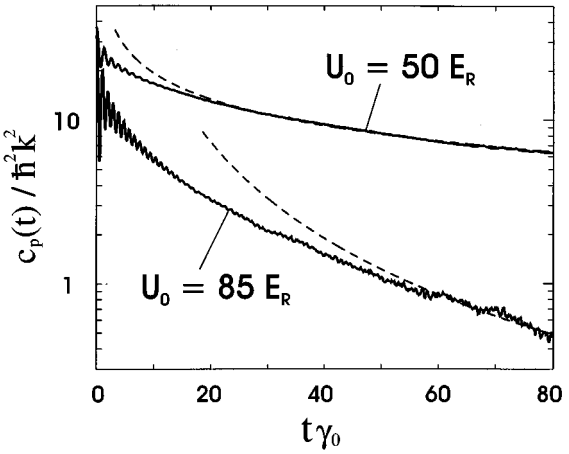

FIG. 6. Stationary momentum correlation function [in units of $(\hbar k)^2$] vs time [in units of optical pumping times] for $\gamma_0 = 3\omega_R$. The solid lines correspond to the full quantum-mechanical treatment (quantum Monte Carlo method) described in Appendix A. The dashed lines correspond to a $ct^{-\mu}$ fit where c was fitted and μ was calculated according to the semiclassical treatment of Sec. III.

$$c_p(t) = \lim_{T\to\infty}\langle\hat{p}(T), \hat{p}(T+t)\rangle_{\text{sym}}. \tag{34}$$

We thus find the above-mentioned relation,

$$D_z = \frac{1}{M^2}\int_0^\infty d\tau c_p(t), \tag{35}$$

between the spatial diffusion constant D_z and the time integral over the momentum correlation function $c_p(t)$. It is now obvious that a divergence of the spatial diffusion constant is related to a divergence of the time integral of the momentum correlation function. This means that if a certain threshold exists at which the spatial diffusion behavior switches from Gaussian to anomalous diffusion, then the long time behavior of the momentum correlation function must switch from integrable (decaying faster than t^{-1}) to nonintegrable (decaying slower than t^{-1}).

In the following we will restrict ourselves to a $\frac{1}{2}\rightarrow\frac{3}{2}$ transition. A generalization to more complicated transitions is straightforward. The results of QMC simulations are shown in Fig. 6. It is worth mentioning here that in order to calculate these correlation functions we had to use a momentum grid that is considerably larger than the one we used in order to calculate the steady-state momentum distribution in the molasses [7]. For this kind of simulation a momentum grid covering the range $[-64\hbar k, 64\hbar k]$ gives excellent results. In order to produce Fig. 6 we had to use a grid twice as large. As will be shown below this is necessary due to the fact that the slowly decaying tails of the momentum correlation function are made by high-momentum particles.

The solid lines in Fig. 6 correspond to the momentum correlation function as calculated with the rigorous quantum-mechanical method described in Appendix A. We chose two different potential depths, which are both below the threshold for Gaussian diffusion as predicted in Ref. [6]. However, as the analysis in the forthcoming section will show we

rather have to expect this divergence to occur at a somewhat lower U_0, namely, $61.5E_R$. Therefore the two potential depths correspond to above ($85E_R$) and below ($50E_R$) the Gaussian diffusion threshold. The oscillating behavior of the momentum correlation function for small times is due to oscillations of the atom in the light shift potential. Due to the randomness of the momentum kick imposed on the atom by spontaneously emitted photons the momentum decorrelates and the correlation function decreases to zero.

Two observations can be made from Fig. 6. Firstly, the correlation function for the shallow potential is larger than the one for the deeper potential, indicating that the diffusion constant (in case it exists) is at least larger. This confirms the trend for small potential depths that we have seen in Fig. 4. Secondly, a $t^{-\mu}$ fit to the plots indicates that the correlation function for $U_0=85E_R$ decays approximately as t^{-2}, being integrable, whereas the correlation function for $U_0=50E_R$ decays approximately as $t^{-0.5}$, being nonintegrable. However, the results of Fig. 6 are numerical in nature and it is difficult to establish whether the correlation functions already reveal their asymptotic long-time behavior, which we assumed as our justification for a $t^{-\mu}$ fit. The correlation functions might still be decaying, for example, exponentially for times $t\gamma_0>80$ in which case they would both be integrable.

In summary, we find that the increase of the spatial diffusion constant when going to smaller potential depths can be seen in the momentum correlation function as slowly decaying tails. We also find numerical evidence that there exists a certain value U_0^{crit} below which $c_p(t)$ decreases so slowly that the spatial diffusion constant diverges, indicating the onset of an anomalous diffusion behavior.

A direct consequence of long momentum correlations is that the atom retains its momentum state for a rather long time. This in return corresponds to a motion over a large distance. A look at the trajectory in Fig. 1 immediately confirms this: the distance that the atom travels (and therefore the spatial diffusion) is dominated by these long flights whereas those parts of the trajectory where the atom is trapped in the potential wells do not contribute significantly. Mathematically this means that the position of the atom after finishing its nth flight is a random variable that is equal to the sum of independent (and identical) random variables corresponding to the flight distance of the jth flights ($j=1,\ldots,n$). Whether the resulting distribution of this random variable (i.e., the shape of the atomic cloud) in the limit $t\to\infty$ is Gaussian or follows a Lévy law depends critically on the distribution of the flight distances and flight times. To be more specific, it depends on the asymptotic behavior of these distribution functions [10] for large distances and times, respectively.

During the flight period the energy of the atom is well above the maxima of the optical potentials so that it sees these potentials only in an averaged way. This allows us to use a very simple semiclassical picture in order to study the characteristics of these flights. In the following section we will use this simple approach in order to justify the aforementioned asymptotic behavior of the momentum correlation function [i.e., $c_p(t)\sim ct^{-\mu}$ as $t\to\infty$], to derive a relation for the critical exponent μ, and to calculate the asymptotic behavior of the distribution of flight distances for very long flights.

III. SEMICLASSICAL TREATMENT USING FOKKER-PLANCK EQUATIONS

As mentioned in Sec. II C the characteristics of the diffusion are shaped by particles that are flying over large distances and that therefore have an energy well above the barrier between neighboring potential wells. These particles can be well described using Fokker-Planck equations [2,21,3] (see also Sec. IV).

A. Kramers equations for the atomic motion above barrier

In this section we will model the atoms in the molasses by the standard Kramers equation to describe 1D laser cooling of atoms with a $J_g=\frac{1}{2}\to J_e=\frac{3}{2}$ Zeeman substructure in a lin$\perp$lin laser configuration (Sisyphus cooling) under the assumption of negligible spatial modulation [14,21]

$$\left(\partial_t+\partial_z\frac{p}{M}\right)W(z,p,t)=\partial_p\{[-F(p)+D(p)\partial_p]W(z,p,t)\}, \tag{36}$$

with the force

$$F(p)=-\frac{\overline{\alpha p}}{1+(p/p_c)^2} \tag{37}$$

and the momentum diffusion coefficient

$$D(p)=D_1+\frac{D_2}{1+(p/p_c)^2}. \tag{38}$$

The choice for the coefficients $\overline{\alpha}$, D_1, and D_2 varies in the literature. We use the following set that differs from the one used in Ref. [6] (which is actually the reason why our prediction for the diffusion threshold differs from the one found there):

$$\frac{p_c}{\hbar k}=\frac{2}{9}\frac{\gamma_0}{\omega_R}=\frac{2}{9}\frac{\hbar\Gamma s_0}{4E_R}, \tag{39}$$

$$\frac{\overline{\alpha}}{\omega_R}=3\frac{U_0}{\hbar\gamma_0}=6\frac{|\Delta|}{\Gamma}, \tag{40}$$

$$\frac{D_1}{(\hbar k)^2\omega_R}=\frac{82}{45}\frac{\gamma_0}{\omega_R}=\frac{41}{90}\frac{\Gamma s_0}{\omega_R}, \tag{41}$$

$$\frac{D_2}{(\hbar k)^2\omega_R}=\frac{U_0^2}{\hbar\gamma_0 E_R}=\frac{\hbar|\Delta|s_0}{E_R}\frac{|\Delta|}{\Gamma}. \tag{42}$$

This choice of parameters nicely reproduces the momentum distribution that we find from the quantum Monte Carlo simulations. Especially the behavior of the wings of this distribution is predicted very accurately.

From a mathematical point of view it is advantageous to generalize the Kramers equation (36) to

$$\left(\partial_t+\partial_z\frac{p}{M}\right)W(z,p,t)=\partial_p\{[-F(p)+D_1\partial_p]W(z,p,t)\}, \tag{43}$$

where the momentum diffusion coefficient D_1 is independent of p and the force $F(p)$ is antisymmetric and has the asymptotic behavior

$$F(p)\to-\alpha/p \quad \text{for } p\to\pm\infty, \tag{44}$$

but is otherwise not explicitly specified. We would like to note that Eq. (36) is indeed covered by Eq. (43) even though we assume a *constant* momentum diffusion coefficient D_1 in Eq. (43), whereas $D(p)$ is explicitly momentum dependent in Eq. (36). This is due to the fact that one can eliminate the p dependence of the momentum diffusion coefficient (38) according to Ref. [13] without changing the asymptotic behavior of $F(p)$.

The reason for the generalization (43) is that—as will turn out later—only atoms with very large momenta are responsible for the asymptotic expansion of the momentum correlation function for large times.

The explicit form of the coefficient α is derived from Eq. (42):

$$\frac{\alpha}{(\hbar k)^2\omega_R}=\frac{4}{27}\frac{U_0\gamma_0}{E_R\omega_R}=\frac{1}{54}\frac{s_0^2\hbar|\Delta|\Gamma}{E_R\omega_R}. \tag{45}$$

B. Momentum correlation function

In this subsection we are interested in the long-time behavior of the momentum correlation function of the particles described by (43). It is convenient to eliminate the z dependence by integrating over space (assuming that the spatial distribution drops off sufficiently fast as $z\to\infty$). We thereby get the one-dimensional Fokker-Planck equation

$$\partial_t W(p,t)=\partial_p[-F(p)W(p,t)]+D_1\partial_p^2 W(p,t), \tag{46}$$

which has the stationary solution

$$W_{\rm st}(p)=Ne^{-\int_0^p d\zeta F(\zeta)/D_1}, \tag{47}$$

where N is some normalization constant.

The stationary momentum correlation function for (46) is given by [13]

$$c_p(t)=\int dp\ pw(p,t). \tag{48}$$

where $w(p,t)$ obeys the Fokker-Planck equation (46) with initial condition $w(p,0)=pW_{\rm st}(p)$.

In order to calculate the asymptotic expansion of $c_p(t)$ as $t\to\infty$ we first approximate the force $F(p)$ by

$$F_a(p)=\begin{cases}F(p), & |p|<p_a\\ -\alpha/p, & |p|>p_a,\end{cases} \tag{49}$$

where p_a is chosen sufficiently large in order to make the error small [which is always possible due to (44)]. As will be shown in Appendix B such a force leads to a momentum correlation function having the asymptotic expansion

$$c_p(t)\sim p_a^{2\mu+3}W_{\rm st}(p_a)\frac{\pi(2\mu-3)^\mu}{\alpha^\mu 4^{\mu+1}\mu(\mu+1)\Gamma(\mu+2)}t^{-\mu}, \tag{50}$$

where the critical exponent μ is given by

$$\mu=\frac{\alpha}{2D_1}-\frac{3}{2}. \tag{51}$$

In order to get rid of the artificially introduced approximation (49) we perform the limit $p_a\to\infty$ and thus recover the original problem (46). It is easy to check using (47) and (44) that the first two factors go to a constant in this limit. We therefore find that the asymptotic behavior of the momentum correlation function for (46) is proportional to $t^{-\mu}$ with a proportionality constant that depends on the detailed form of the force $F(p)$. In contrast to that, μ depends only on the ratio α/D_1 and therefore only on the large momentum behavior of $F(p)$.

It is now easy to see that Gaussian spatial diffusion is found whenever $\mu>1$ and that the spatial diffusion constant diverges (anomalous diffusion) if $\mu<1$. Using the expressions (45) we can write

$$\mu=\frac{5}{123}\frac{U_0}{E_R}-\frac{3}{2}, \tag{52}$$

and find the threshold for Gaussian diffusion at $U_0^{\rm crit}=61.5E_R$, as already mentioned in the previous section. Note that this number is only valid for an atom with a $J_g=\frac{1}{2}\to J_e=\frac{3}{2}$ Zeemann substructure in a 1D lin⊥lin laser configuration.

We are now able to revisit Fig. 6 in order to check how the prediction for the long-time behavior of the momentum correlation function derived in this section compares with the full quantum-mechanical treatment of Sec. II C. We have now not only a justification for a $t^{-\mu}$ fit to the graphs in Fig. 6, but we are also able to relate μ to the potential depth. For the parameters given in this figure we find that $\mu=0.533$ for the shallow potential and $\mu=1.96$ for the deep one. We have fitted the proportionality constant (which we cannot calculate with a semiclassical treatment) and the resulting graphs are shown as dashed lines in Fig. 6. The good agreement indicates that the diffusion threshold exists in the full quantum-mechanical system and is not only an artifact of a semiclassical treatment.

C. Distribution of flight distance and Lévy walks

Up to now we have shown that there exists a critical potential depth below which the spatial diffusion constant diverges, indicating that the diffusive behavior of our system shows a transition from Gaussian to anomalous. We already mentioned in the Introduction that this transition is caused by a substantial change of the character of the microscopic motion of the atoms in the molasses. The characterization of this motion will be the main concern of the rest of this section.

We found so far that the decision between Gaussian and anomalous diffusion is made by atoms that wander high up in momentum space, thereby flying over a large distance. It seems therefore worthwhile to study the distribution of this

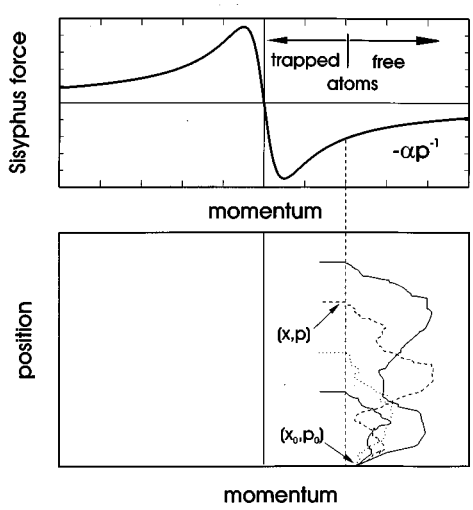

FIG. 7. Schematic plot illustrating the distribution of flight distances. The upper plot shows the momentum dependence of the cooling force. The lower plot shows some stochastic trajectories in phase space. Atoms are supposed to be trapped (and therefore inert) as soon as their momentum falls below a certain threshold (indicated by the dashed line) but are allowed to wander in space if their momentum is above threshold. Note that the starting point of all trajectories has a slightly larger momentum than the trapping momentum in order to produce nontrivial first-exit-point distributions.

flight distance under the following assumptions: (1) Atoms with a momentum below a certain threshold p_0 are trapped in the optical potential wells and do not wander around. (2) Atoms that (in the course of their random walk) cross this threshold from below start to wander around in both momentum and position space, until they cross the threshold again (this time from above) which results in their capture. During this phase of their random walk the atoms see only the asymptotic part of the force, i.e., $F(p) \approx -\alpha/p$. This situation is sketched in the upper part of Fig. 7.

This model is a generalization of the Kramers equation (43) that can be accounted for by replacing

$$\partial_z \left[\frac{p}{M} W(z,p,t) \right] \rightarrow \partial_z [v(p) W(z,p,t)] \tag{53}$$

with the velocity function

$$v(p) = \begin{cases} 0, & |p| < p_0 \\ p/M, & |p| > p_0 \end{cases}, \tag{54}$$

where the cutoff for spatial motion occurs whenever the kinetic energy is less than the maximum of the potential, i.e., $p_0^2/2M = 4U_0/3$. We have used this generalization of the Kramers equation to calculate spatial diffusion constant following the procedure given in Ref. [6] and found a suppression of the diffusion by a factor of 2–3 as compared to the original Kramers equation (43).

However, in the rest of this section we are only interested in the distribution of the flight distances and therefore in the motion of the atoms above the threshold p_0. This amounts to calculating the probability of an atom that crosses the threshold p_0 at a certain position z_0 to exist through the p_0 line for the first time at point z, the distance of the flight being $z - z_0$. This definition of the distribution of flight distances is a very appealing one, but leads to a Dirac δ distribution around $z = z_0$ meaning that *any* particle immediately crosses p_0 again [22]. In order to get nontrivial results we have to lower the threshold for the second crossing by a small but finite value. This is depicted in the lower part of Fig. 7.

As will be shown in Appendix C the distribution of flight distances (or—as it is mathematically called—the distribution of first exit points) for our problem has the asymptotic expansion

$$\pi_e(z,p,z_0,p_0) \sim \frac{1}{3^{2\nu}} \frac{(3\nu+1)^\nu}{\Gamma(\nu)} \frac{p_0^{3\nu} - p^{3\nu}}{(z-z_0)^{\nu+1}} \tag{55}$$

with a critical parameter ν that is related to the potential depth via

$$\nu = \frac{\alpha}{3D_1} + \frac{1}{3} = \frac{10}{369} \frac{U_0}{E_R} + \frac{1}{3}. \tag{56}$$

We thus find that the distribution of flight distances possess both first and second moments for $\nu > 2$ whereas the second moment ceases to exist below $\nu = 2$. This threshold coincides with the threshold for Gaussian diffusion predicted in Sec. III B and one is tempted to assign the onset of anomalous diffusion to the existence of Lévy flights in the atomic trajectories. Indeed, the trajectories show the self-similarity mentioned in the Introduction, i.e., the domination by single, rare events that is typical for Lévy flights. However, since the system studied here is intrinsically a dynamical one we also have to consider the time it takes the atom to finish this long flight. We have calculated the parameter range in which the first and second moment of the distribution of the flight times exist (see Appendix D) and the result is shown in Fig. 8.

We find that above the Gaussian diffusion threshold $\mu = 1$ (which for the case of a $J_g = \frac{1}{2} \rightarrow J_e = \frac{3}{2}$ atom in a 1D lin$\perp$lin laser configuration is at $U_0^{\text{crit}} = 61.5 E_R$) both the distribution of flight distances and of flight durations possess finite expectation values and variances for these (not independent) random variables, leading to a Gaussian type of diffusion. Below this threshold we find a regime ($0 < \mu < 1$) for which the distribution of flight times still possess finite first and second moments, but the distribution of flight distances has an infinite variance. The anomalous diffusion in this regime is indeed caused by Lévy walks that take a finite time (i.e., last on a certain time scale). These flights are thus very close to what is mathematically defined as Lévy flights.

Below this we find a regime ($1 < \nu < \frac{4}{3}$) in which also the variance of the flight times ceases to exist. We thus encounter the situation in which the atoms show Lévy walks that are in some sense longer than the ones mentioned before (in a fractal sense they are closer to a one-dimensional trajectory [11]), but that at the same time last for arbitrarily long times. This situation corresponds to a Lévy flight in both space and time. Interestingly, this regime coincides with the one where no expectation value for the kinetic energy of the atoms exists.

Below this regime the expectation value for the flight distance diverges and eventually also the first moment of the

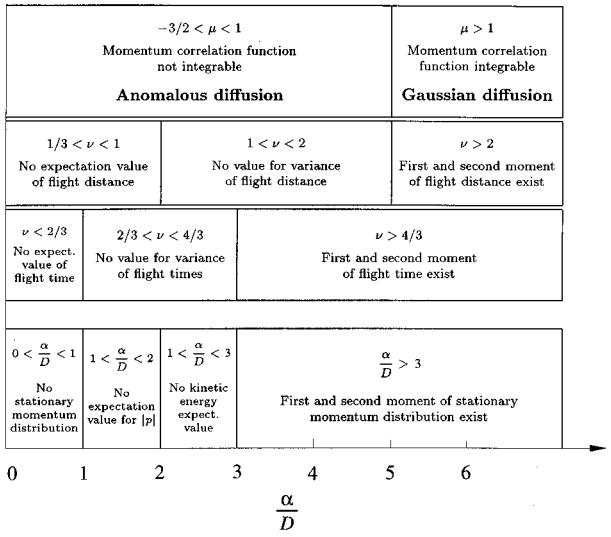

FIG. 8. A map of the various regimes of nonexistence of the first and second moments of several distribution functions discussed in the text as a function of the parameter α/D_1. The uppermost block corresponds to the moments of the momentum correlation function (Sec. III B). The two block below that corresponds to the distribution of flight distance and flight times, respectively. The last block (set apart from the others) gives the moments of the stationary momentum distribution. The shaded region corresponds to the regime where no variance of the flight distance exists, but the distribution of flight times possesses both first and second moments.

flight time ceases to exist leading to a nonexistence of a stationary momentum distribution (the molasses is heating).

D. Influence of Doppler forces: Truncation of the Lévy walks

In the last subsection we would like to discuss whether the Lévy walks found above can be observed experimentally. As mentioned before the experiment of Ref. [6] is not really suited for reasons already stated. However, one could think of an experimental setup very similar to the one used therein that tries to resolve the non-Gaussian wings (i.e., the Lévy distribution) of the spatial distribution. This approach has to face several experimental challenges: firstly, the relative phase of the various laser beams needs to be stabilized very precisely in order to produce a time-independent optical potential. Secondly and more important, the experiment must be set in a detuning regime in which Doppler forces can be neglected on the time scale of the experiment. This is due to the following effect. In the previous discussion we have assumed a cooling force that decays as p^{-1} with increasing momentum. The occurrence of Lévy walks results exactly from this behavior. But in a realistic situation a force with this behavior exists only in a momentum regime, where the atoms have a negligible Doppler shift. This is an important assumption made during the adiabatic elimination of the excited state, which was used throughout this paper. However, since the long-time behavior of the momentum correlation function is made by faster and faster particles they will at some stage violate this assumption and they will start to experience the strong Doppler force. This force prevents them from climbing higher in momentum space and therefore effectively cuts off the momentum correlation function. In order to demonstrate this we have numerically calculated the momentum correlation function of Eq. (36) with the modified force

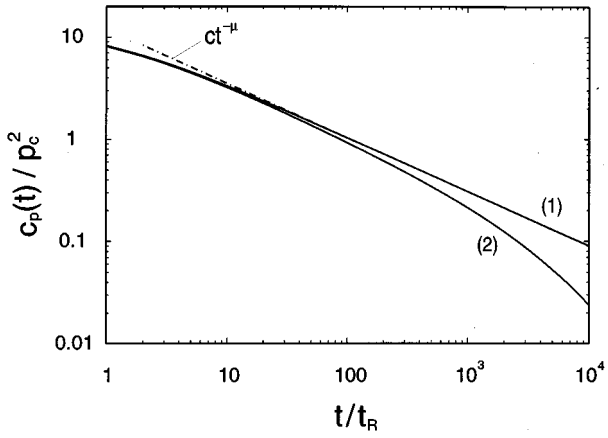

FIG. 9. Numerical calculation of the momentum correlation function without (1) and with (2) Doppler correction Eq. (57). The dash-dotted line gives the asymptotic behavior as calculated in Sec. III B. Parameters: $U_0 = 50E_R$, $\gamma_0 = 10\omega_R$, $\alpha_D = 10^{-5}\omega_R^{-1}$.

$$F^{\text{Doppler}}(p) = F(p) - \alpha_D p, \tag{57}$$

where the first-order expansion of the Doppler Force is given by

$$\alpha_D \omega_R = \frac{128}{9} \frac{\hbar \gamma_0^3}{\Gamma^2 U_0}. \tag{58}$$

The result is shown in a double-logarithmic plot in Fig. 9. The upper solid curve corresponds to neglecting Doppler forces. After a short transient on the order of approximately $10t_R$ the momentum correlation function reaches its asymptotic behavior $ct^{-\mu}$, which is indicated by the dashed-dotted line. The lower curve corresponds to the correlation function with the first-order Doppler correction included. The initial transient is more or less identical, however, the correlation function follows the $ct^{-\mu}$ only for a certain time (which is for the parameters used in Fig. 9 approximately $100t_R$). For larger times the correlation functions drop considerably faster. This results in the effect that the initially nonintegrable correlation functions are now rendered integrable. We recover a Gaussian type of diffusion where the original Lévy walks (which in the idealized semiclassical model caused the anomalous diffusion) are effectively truncated as soon as they try to fly beyond a certain critical distance [23]. The point at which this cutoff is effective and thus the time scale on which the diffusion is anomalous depends very much on the detuning that one is using in the experiment, larger detunings leading to a later truncation of the correlation function and therefore to a larger spatial diffusion constant. But on the other hand it could be exactly this kind of effect that might lead to an indirect experiment that is able to detect the Lévy flights.

Another experiment that one can think of is the (indirect) detection of the Lévy flights due to their influence on the

narrow central feature in the weak probe absorption spectrum due to recoil-induced resonances [24].

IV. TWO-DIMENSIONAL OPTICAL LATTICES

In this section we will present a semiclassical examination of two two-dimensional laser configurations in order to study whether the Lévy walks that we found in the one-dimensional case also show up in higher-dimensional molasses. As we will show this behavior does indeed exist but there are also some new features depending on the laser fields used to set up the optical molasses These new effects compete with the Lévy walks and can in certain cases (as, e.g., in the second case studied below) overpower them and lead to a completely new type of long-time behavior.

These new effects come from a property that is common to all higher-dimensional molasses: The laser field has no rotational symmetry and therefore the light force which the atom experiences depends crucially on the direction in which the atom propagates. This can lead to a very different behavior for particles that propagate into a certain direction as compared to atoms that propagate into a slightly different direction. This anisotropy of the atomic motion along certain channels can for some geometries establish an important loss mechanism for optical molasses in higher dimensions.

The master equation we consider for two-dimensional Sisyphus cooling can be written in the form (excited states have been adiabatically eliminated)

$$\dot{\rho}_{gg}=-\frac{i}{\hbar}(h_{\rm eff}\rho_{gg}-\rho_{gg}h_{\rm eff}^{\dagger})+\sum_{\sigma,\sigma'=0,\pm}\frac{\gamma_0}{2\pi}\int d\Omega_{\boldsymbol{n}}N_{\sigma\sigma'}(\boldsymbol{n}) \times[B_{\sigma}(\hat{\boldsymbol{x}})e^{-ik\boldsymbol{n}\cdot\hat{\boldsymbol{x}}}]\rho_{gg}[B_{\sigma'}^{\dagger}(\hat{\boldsymbol{x}})e^{ik\boldsymbol{n}\cdot\hat{\boldsymbol{x}}}], \tag{59}$$

with effective Hamiltonian

$$h_{\rm eff}\equiv\frac{\hat{P}^2}{2M}+\frac{\hbar s_0}{2}\left(\Delta-i\frac{\Gamma}{2}\right)\mathscr{D}(\hat{\boldsymbol{x}})\mathscr{D}^{\dagger}(\hat{\boldsymbol{x}}) \tag{60}$$

and angular distributions for the spontaneously emitted photons

$$N_{\sigma\sigma'}(n)=\tfrac{3}{4}(\delta_{\sigma\sigma'}-n_{\sigma}^{*}n_{\sigma'}) \tag{61}$$

with $n_0=\cos(\theta)$ and $n_{\pm}=\mp(1/\sqrt{2})\sin(\theta)e^{\pm i\phi}$. We consider electric fields with a positive frequency part of the form

$$\boldsymbol{E}_{(x)}^{(+)}=\mathscr{E}[S(\boldsymbol{x})\boldsymbol{e}_{+}+C(\boldsymbol{x})\boldsymbol{e}_{-}]. \tag{62}$$

This guarantees that no ground-state coherences are build up in a $\frac{1}{2}\rightarrow\frac{3}{2}$ optical transition. These configurations are thus assumed to consist of laser fields with polarizations concentrated in a plane perpendicular to some given direction $\boldsymbol{e}_0$. We entirely restrict our discussion on a $\frac{1}{2}\rightarrow\frac{3}{2}$ optical transition in the following. The optical potential $U(\boldsymbol{x})$ can be written in the form

$$U(\boldsymbol{x})=-\tfrac{1}{3}U_0\{|+\rangle\langle+|+|-\rangle\langle-|\}[|S(\boldsymbol{x})|^2+|C(\boldsymbol{x})|^2] -\tfrac{2}{3}U_0\{|+\rangle\langle+\|S(\boldsymbol{x})|^2+|-\rangle\langle-\|C(\boldsymbol{x})|^2\}. \tag{63}$$

After transforming the master equation into the Wigner picture, and subsequent expansion in orders of $\hbar\boldsymbol{k}$ (up to second order), we get a bipotential equation for the two components of the Wigner operator (the ground-state coherences vanish)

$$\left[\frac{\partial}{\partial t}+\frac{\boldsymbol{p}}{M}\cdot\boldsymbol{\nabla}_{\boldsymbol{x}}\right]f_{\pm}(\boldsymbol{x},\boldsymbol{p},t)=\langle\pm|\mathscr{L}^{(0)}W_{gg}(\boldsymbol{x},\boldsymbol{p},t)|\pm\rangle +\langle\pm|\mathscr{L}^{(1)}W_{gg}(\boldsymbol{x},\boldsymbol{p},t)|\pm\rangle +\langle\pm|\mathscr{L}^{(2)}W_{gg}(\boldsymbol{x},\boldsymbol{p},t)|\pm\rangle, \tag{64}$$

with $f_{\pm}(\boldsymbol{x},\boldsymbol{p},t)$ denoting the diagonal components of the Wigner operator

$$f_{\pm}(\boldsymbol{x},\boldsymbol{p},t)=\langle\pm|W_{gg}(\boldsymbol{x},\boldsymbol{p},t)|\pm\rangle. \tag{65}$$

The explicit form for the right-hand side of Eq. (64) for electric fields of the form Eq. (62) can be found in Appendix E. For semiclassical center-of-mass motion Eq. (64) can be turned into a Fokker-Planck equation for the Wigner function $W(\boldsymbol{x},\boldsymbol{p},t)$ by adiabatic elimination of the internal degrees of freedom [2].

A. Two crossed linear polarized laser beams

The first laser configuration we consider consists of two cross linear polarized lasers propagating in the x and y directions, respectively with a phase difference ϕ. This configuration was used in the 2D experiments of Ref. [16]. The positive frequency part of the electric field is given by

$$\boldsymbol{E}^{(+)}(\boldsymbol{x})=2\mathscr{E}[\cos(kx)\boldsymbol{e}_y+e^{i\phi}\cos(ky)\boldsymbol{e}_x]. \tag{66}$$

The atomic motion is defined with respect to the optical bipotential

$$U_{\pm}(x,y)=-\frac{8U_0}{3}[\cos^2(kx)+\cos^2(ky) \pm\sin(\phi)\cos(kx)\cos(ky)]. \tag{67}$$

As discussed in Ref. [16] the spatial pattern of the light polarization is analogous to the one-dimensional lin⊥lin molasses discussed in the previous sections if one chooses a phase shift of $\phi=90°$. In this case there exists a 2D array of straight lines parallel to the z axis where the light exhibits circular polarization with alternating sign and continuously changes to linear polarization when one moves away from these locations. We will therefore restrict the following analysis to this case. The above-barrier motion is fully determined by the semiclassical theory (we have again neglected the Doppler cooling mechanism in the adiabatic elimination of the excited states):

$$\left(\frac{\partial}{\partial t}+\frac{\boldsymbol{p}}{m}\cdot\frac{\partial}{\partial \boldsymbol{x}}\right)W(\boldsymbol{x},\boldsymbol{p},t)=-\frac{\partial}{\partial \boldsymbol{p}}[\boldsymbol{F}(\boldsymbol{p})W(\boldsymbol{x},\boldsymbol{p},t)]+\sum_{i=x,y}\frac{\partial^2}{\partial p_i^2}[D_{ii}W(\boldsymbol{x},\boldsymbol{p},t)]. \tag{68}$$

In the one-dimensional case we have observed that the character of the above-barrier motion, which dominates the spatial diffusion of an initially localized wave packet, is entirely determined by the large-momentum behavior of the semiclassical cooling force. It is therefore natural to calculate a similar expansion of the force in two dimensions, keeping in mind anisotropic effects.

An expansion in powers of $1/v$ reveals the leading behavior

$$\boldsymbol{F}(\boldsymbol{v})\sim-\frac{32\gamma_0U_0}{27}\left\{\frac{\boldsymbol{e}_x+\boldsymbol{e}_y}{v_x+v_y}+\frac{\boldsymbol{e}_x-\boldsymbol{e}_y}{v_x-v_y}\right\} \tag{69}$$

if the atomic velocity is *not* in the vicinity of the channels $v_y=v_x$ and $v_y=-v_x$. This expansion of the force for atoms with large atomic velocities shows an anisotropy with a divergence as one goes towards the channels $v_y=v_x$ and $v_y=-v_x$, which are—in contrast to the next case—not aligned with the incident laser beams but lay symmetrically in between them (cf. Fig. 10). In the vicinity of the channel $k|v_y-v_x|\leqslant\gamma_0$ the semiclassical force can be expanded for $k|\boldsymbol{v}|\gg\gamma_0$,

$$\boldsymbol{F}(\boldsymbol{v})\sim-\frac{32\gamma_0U_0}{27}\left\{\frac{\boldsymbol{e}_x-\boldsymbol{e}_y}{v_x-v_y}\frac{k^2(v_x-v_y)^2}{256\gamma_0^2/81+k^2(v_x-v_y)^2}+\frac{\boldsymbol{e}_x+\boldsymbol{e}_y}{v_x+v_y}\left[1-\frac{128\gamma_0^2/81}{256\gamma_0^2/81+k^2(v_x-v_y)^2}\right]\right\}, \tag{70}$$

which clearly shows that the force in the channel (whose width is proportional to γ_0/k) is always cooling, i.e., is pointing towards the origin $|\boldsymbol{v}|=0$. But it decreases at the same time with the inverse velocity along the channel We therefore encounter the following behavior for atoms above barrier in this configuration: High velocity atoms are cooled and at the same time attracted towards the four channels. Once they reach these channels they feel a perpendicular force component [first term in (70)] that depends only on v_x-v_y, i.e., on the distance to the channel. In contrast to that the force parallel to the channel [second line in (70)] depends on the norm of the velocity, i.e., on the distance along the channel. The atoms are thus strongly confined to a quasi-one-dimensional subspace along which they feel the force

$$\boldsymbol{F}(\boldsymbol{v})\sim-\frac{8\sqrt{2}\gamma_0U_0}{27}\frac{\boldsymbol{e}_x+\boldsymbol{e}_y}{|\boldsymbol{v}|}=-\beta\frac{\boldsymbol{e}_x+\boldsymbol{e}_y}{|\boldsymbol{v}|}. \tag{71}$$

This situation is completely analogous to the one-dimensional case as discussed in the previous sections. The force along the four channels allows (due to its $1/|\boldsymbol{v}|$ dependence) the existence of Lévy walks for sufficiently shallow optical potentials. Note that these walks lead due to the confinement of the velocity to the channels to almost straight trajectories of the atom in position space.

In Fig. 11 we present the numerical result for the stationary momentum distribution. The four channels are clearly visible. Note that the width of the channels is independent of distance from $|\boldsymbol{v}|=0$ and that the distribution decreases along these channels.

The numerical results were obtained by Monte Carlo simulation of the semiclassical bipotential motion (see Ref. [17]).

In order to study the threshold for Gaussian diffusion we utilize the results derived in Sec. III. The diffusion matrix for high velocities can be approximated by a diagonal matrix with constant coefficients

$$D_{xx}=\frac{97\gamma_0(\hbar k)^2}{90},\quad D_{yy}=\frac{91\gamma_0(\hbar k)^2}{90}, \tag{72}$$

which together with (71) allows us to calculate the critical potential depth in complete analogy to the 1D case. We find

$$\nu=\frac{2\beta}{3(D_{xx}+D_{yy})}+\frac{1}{3}=\frac{10\sqrt{2}}{47}\frac{U_0}{E_R}+\frac{1}{3}, \tag{73}$$

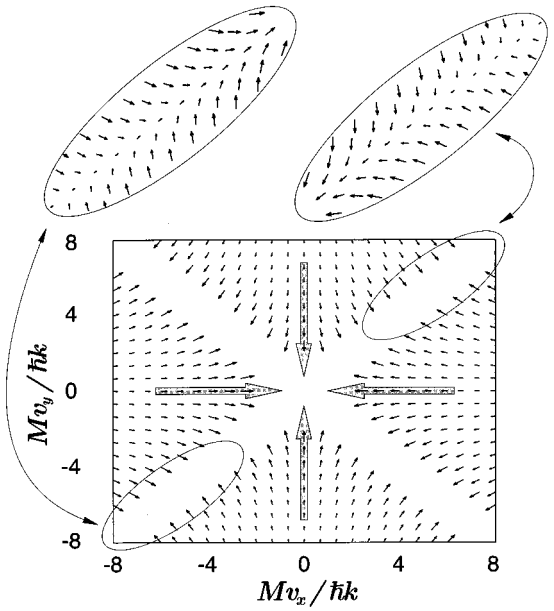

FIG. 10. Vector plot of the semiclassical force in the four-beam configuration according to the expansion (69). The magnified ellipses depict the force close to the channels (70). The gray arrows indicate the directions of the incident laser beams.

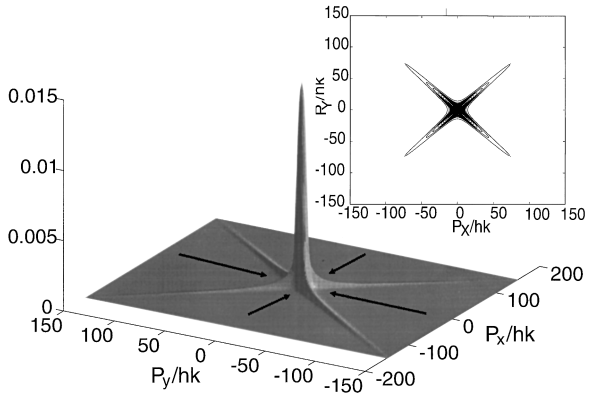

FIG. 11. Stationary momentum distribution in the four-beam optical molasses for the parameters $U_0=40/3E_R$ and $\gamma_0=16/3\omega_R$.

from which we deduce that Lévy flights exist for potential depths below $U_0^{\mathrm{crit}}=16.62E_R$. Note that for potential depths below $U_0\leqslant 3.32E_R$ the distribution of the momentum along the channels is not normalizable and therefore these channels play a role very similar to the escape channels of the three-beam configuration, which we discuss in the following subsection.

B. Three-beam configuration

As in the 2D experiments of Ref. [15], the laser field studied now is composed of three traveling plane waves of equal strength, with coplanar wave vectors, rotated by 120° with respect to each other, and linear polarizations in the common plane. This setup has the advantage that relative phases are irrelevant (even though a fluctuating phase leads to a spatial motion of the optical potential as mentioned before). The positive frequency part of the electric field is given by

$$\boldsymbol{E}^{(+)}(\boldsymbol{x})=E_0\left[\boldsymbol{e}_y e^{i\boldsymbol{k}_1\cdot\boldsymbol{x}}+\left(\frac{\sqrt{3}}{2}\boldsymbol{e}_x-\frac{1}{2}\boldsymbol{e}_y\right)e^{i\boldsymbol{k}_2\cdot\boldsymbol{x}}+\left(-\frac{\sqrt{3}}{2}\boldsymbol{e}_x-\frac{1}{2}\boldsymbol{e}_y\right)e^{i\boldsymbol{k}_3\cdot\boldsymbol{x}}\right], \tag{74}$$

with wave vectors

$$\boldsymbol{k}_1=k\boldsymbol{e}_x,\quad \boldsymbol{k}_2=-\frac{k}{2}\boldsymbol{e}_x-\frac{\sqrt{3}k}{2}\boldsymbol{e}_y,$$

$$\boldsymbol{k}_3=-\frac{k}{2}\boldsymbol{e}_x+\frac{\sqrt{3}k}{2}\boldsymbol{e}_y. \tag{75}$$

For small saturation $s_0\ll 1$ we can again derive a Fokker-Planck equation for the above-barrier motion, which is now defined with respect to the optical bipotential

$$U_{\pm}(x,y)=-\frac{4}{3}U_0\left\{\left[1+\sin^2\left(\frac{\sqrt{3}}{2}ky\right)-\cos\left(\frac{3}{2}kx\right)\cos\left(\frac{\sqrt{3}}{2}ky\right)\right]\pm\frac{\sqrt{3}}{2}\left[\cos\left(\frac{3}{2}kx\right)\sin\left(\frac{\sqrt{3}}{2}ky\right)-\sin\left(\frac{\sqrt{3}}{2}ky\right)\cos\left(\frac{\sqrt{3}}{2}ky\right)\right]\right\}. \tag{76}$$

The nondiagonal terms in the diffusion matrix do not enter the equation for the above-barrier motion and the diagonal elements are dominated by the velocity-independent coefficients

$$D_{xx}=\frac{183}{90}\gamma_0(\hbar k)^2,\quad D_{yy}=\frac{147}{90}\gamma_0(\hbar k)^2. \tag{77}$$

In analogy to the previous configuration we expand the semiclassical cooling force in powers of $1/v$,

$$\boldsymbol{F}(\boldsymbol{v})\sim-\frac{2U_0\gamma_0}{9}\left[\boldsymbol{e}_y\frac{1}{2v_y}+\left(\frac{\sqrt{3}}{2}\boldsymbol{e}_x-\frac{1}{2}\boldsymbol{e}_y\right)\frac{1}{\sqrt{3}v_x-v_y}+\left(\frac{\sqrt{3}}{2}\boldsymbol{e}_x+\frac{1}{2}\boldsymbol{e}_y\right)\frac{1}{\sqrt{3}v_x+v_y}\right], \tag{78}$$

which can be written in the form

$$\boldsymbol{F}(\boldsymbol{v})\sim-\nabla_{\boldsymbol{v}}V(\boldsymbol{v}) \tag{79}$$

by defining a potential

$$V(v_x,v_y)=\frac{U_0\gamma_0}{9}\ln(|v_y||3v_x^2-v_y^2|). \tag{80}$$

A vector plot of this force is shown in the main plot of Fig. 12. This expansion of the force for atoms with large atomic velocities shows again an anisotropy, but now the divergence occurs along the three lines that coincide with the three directions of the laser beams—in contrast to the previous case. This indicates that the approximation used to derive (78) breaks down along these channels and hence we have left these regions blank in the plot.

A striking feature of the vector field depicted in Fig. 12 is that the momentum of an atom with large energy is drawn towards the center due to a Sisyphus cooling mechanism, but is rotated at the same time towards six channels (i.e., the star-shaped blank region in the main plot of Fig. 12). The atom is therefore not cooled all the way down to small momenta but it rather attracted to the nearest channel. According to approximation (78) the component of the force parallel to the six channels vanishes and therefore the atom does not feel a cooling force once it reaches the channel. However, the force perpendicular to the channels diverges and therefore we have to use a different expansion in order to study the behavior of the force close to these channels.

In order to clarify this point we again expand the cooling force in the vicinity of the channels. Let us consider the

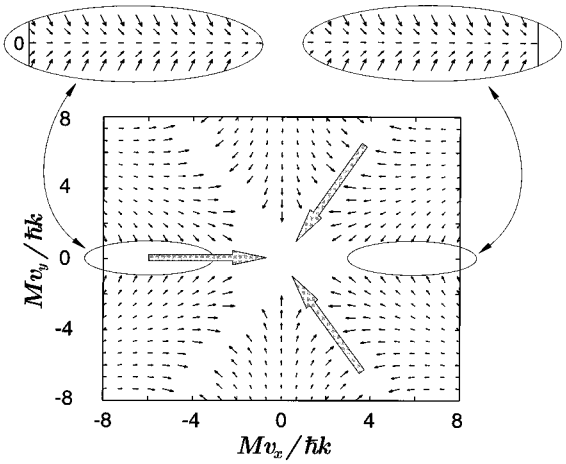

FIG. 12. Vector plot of the semiclassical force in the three-beam configuration according to the expansion (78). The magnified ellipses depict the force close to the channels (81). The gray arrows indicate the directions of the incident laser beams.

regime in velocity space that is characterized by $k|v_y| \leqslant \gamma_0$ and $k|\boldsymbol{v}| \gg \gamma_0$. Along the direction of the laser beam $\boldsymbol{k}_1$ we observe a position-dependent alignment (i.e., a difference in the populations of the two ground states) that gives rise to a net force along the channel $\boldsymbol{k}_1$:

$$\boldsymbol{F}(\boldsymbol{v}) \sim \boldsymbol{e}_x \gamma_0 k \left(\frac{51}{613 + 1458(\sqrt{3} k v_y / 2\gamma_0)^2} \right) - \boldsymbol{e}_y \frac{4U_0 k}{3} \left(\frac{(27)^2 \sqrt{3} k v_y / 2\gamma_0}{613 + 1458(\sqrt{3} k v_y / 2\gamma_0)^2} \right). \quad (81)$$

The behavior of this force is magnified in the ellipses in Fig. 12. Atoms with large negative v_x components feel a light pressure force pointing to the right resulting in a total force that pushes the atomic momentum towards $|\boldsymbol{v}| = 0$ depicted in the left magnified ellipses. They are therefore cooled down to small atomic velocities, whereas atoms with positive v_x components are collected into the escape channel $v_y = 0$ and then accelerated to very high atomic velocities (right ellipsis in Fig. 12). These atoms rapidly escape from the molasses. Hence the name *escape* channels [25]. It is clear that no stationary momentum distribution exists (unless we include Doppler effects) and therefore no stationary spatial diffusion behavior is reached in contrast to the channels of the previously considered crossed-beam configuration.

Figure 13 shows the numerical result for the quasistationary momentum distribution (atoms that leave the simulation grid are fed back at $|\boldsymbol{v}| = 0$) in the three-beam molasses. Note the existence of three escape channels pointing into the directions of the incident laser beams as predicted by the semiclassical investigation above. For a related discussion of the anisotropy aspects in this laser configuration we refer to Ref. [25].

The two different models show that Lévy-flight behavior is not limited to one-dimensional setups. However, due to the inherent anisotropy of the two- or higher-dimensional setup a variety of other effects exist (such as, e.g., the escape channels of the three-beam configuration) that compete with the Lévy flights. We have demonstrated that these effects can be studied via very simple semiclassical methods. The methodology presented in this paper has therefore applications to a larger class of problems than only the spatial diffusion.

V. CONCLUSION

We have studied the spatial motion of (noninteracting) atoms in a one-dimensional optical lattice provided by two counterpropagating cross-linearly polarized laser beams. The first step in this study was performed with an *ab initio* quantum-mechanical treatment. We used a wave-function Monte Carlo technique with localizing quantum jumps in order to calculate the dependence of the spatial diffusion constant on system parameters and found that the quantum treatment predicts diffusion constants that are considerably lower than the ones obtained from semiclassical methods [6]. We also used the standard Monte Carlo technique in order to calculate momentum correlation functions of the master equation. We found that the momentum correlation function develops slowly decaying tails as the depth of the potential wells of the optical molasses is decreased. This indicates that there exist a certain threshold at which the spatial diffusion switches from Gaussian to anomalous behavior. In a second part we have studied this transition by using a simple semiclassical approach.

Our analysis showed that the microscopic motion of the atom in the molasses is characterized by two very different ''states.'' Firstly, the atom can be trapped in the potential wells and is then inert. Secondly, the energy of the atom can be above the potential barrier in which case the atom is able to move over many wavelengths. Transitions between these two states are stochastically induced by the cooling force (slowing of fast atoms) and its fluctuations (heating due to randomness of spontaneous emission and fluctuations of the atomic dipole moment).

The character of the diffusion depends strongly on the distribution of the flight distances and their variance as well as on the time it takes to complete them. We found that for potential depths above a critical value these distributions have both an expectation and a variance and the resulting motion of the atoms is thus a Gaussian diffusion. For potential depths below the critical value we found that the variance of the distribution of flight distances ceases to exist (while the distribution of flight times still possesses both first and second moments), leading to the onset of anomalous diffusion. This is related to the existence of so-called Lévy walks in the atomic trajectories. We predicted the abovementioned critical potential depth for a $J_g = \frac{1}{2} \rightarrow J_e = \frac{3}{2}$ transition in a 1D lin$\perp$lin laser configuration to be $U_0^{\mathrm{crit}} = 61.5 E_R$. We have also studied a two-dimensional laser configuration and have found that this system also shows Lévy walks, but the threshold for Gaussian diffusion is considerably lower, namely, at $U_0^{\mathrm{crit}} = 16.62 E_R$.

ACKNOWLEDGMENTS

We thank H. J. Kimble and P. Marte for stimulating discussions. This work was supported by the Austrian Science Foundation under Grant No. S06507-PHY.

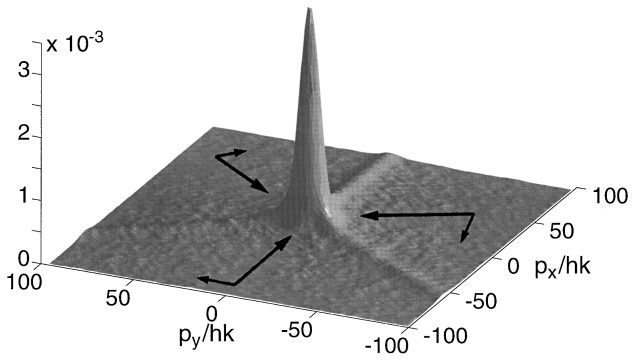

FIG. 13. Quasistationary momentum distribution calculated via Monte Carlo simulation of the 2D bipotential Fokker-Planck equation. Particles that left the grid through the escape channels were fed back at $|\mathbf{p}|=0$. The parameters are $U_0=200/3E_R$ and $\gamma_0=15/2\omega_R$.

APPENDIX A: QMC SIMULATION OF THE MOMENTUM CORRELATION FUNCTION

In this appendix we will show how the momentum correlation function can be calculated within a quantum Monte Carlo wave function approach.

To do this we follow the procedure given in Ref. [7] and define the functional

$$S_f(t)\equiv\int_0^t d\tau\, f(\tau)[\langle\hat{p}(\tau)\hat{p}(t)\rangle+\langle\hat{p}(t)\hat{p}(\tau)\rangle]. \quad \text{(A1)}$$

The momentum correlation function follows from the quantum regression theorem:

$$\langle\hat{p}(\tau)\hat{p}(t)\rangle=\mathrm{tr}_s\hat{p}e^{\mathscr{L}(t-\tau)}[\rho(\tau)\hat{p}] \quad \text{for } \tau<t,$$

$$\langle\hat{p}(t)\hat{p}(\tau)\rangle=\mathrm{tr}_s\hat{p}e^{\mathscr{L}(t-\tau)}[\hat{p}\rho(\tau)] \quad \text{for } \tau<t, \quad \text{(A2)}$$

where $\mathscr{L}$ is the master operator and $\rho(t)$ the density operator according to (11). We can now rewrite (A1) as

$$S_f(t)=\mathrm{tr}_s\hat{p}\rho_1(t) \quad \text{(A3)}$$

with

$$\rho_1(t)=\int_0^t d\tau\, f(\tau)e^{\mathscr{L}(t-\tau)}[\rho(\tau)\hat{p}+\hat{p}\rho(\tau)]. \quad \text{(A4)}$$

The two operators $\rho(t)$ and $\rho_1(t)$ obey the coupled equations

$$\dot{\rho}(t)=\mathscr{L}\rho(t),$$

$$\dot{\rho}_1(t)=\mathscr{L}\rho_1(t)+f(t)[\rho(t)\hat{p}+\hat{p}\rho(t)]. \quad \text{(A5)}$$

Following the arguments given in Ref. [18], $\rho_1(t)$ can be simulated by propagating the pair of wave functions

$$i\frac{d}{dt}|\Phi(t)\rangle=h_{\mathrm{eff}}|\Phi(t)\rangle,$$

$$i\frac{d}{dt}|\Psi(t)\rangle=h_{\mathrm{eff}}|\Psi(t)\rangle+if(t)\hat{p}|\Phi(t)\rangle, \quad \text{(A6)}$$

where $|\Phi(t)\rangle$ is the stochastic system wave function that gives—via stochastic averaging—the solution of the master equation (11), i.e.,

$$\rho(t)=\langle\langle|\Phi(t)\rangle\langle\Phi(t)|/\|\Phi(t)\|^2\rangle\rangle. \quad \text{(A7)}$$

A solution of (A5) can now be calculated by propagating $|\Phi(t)\rangle$ and $|\Psi(t)\rangle$ according to (A6) between quantum jumps who are dictated by the system wave function $|\Phi(t)\rangle$. Both wave functions experience the same quantum jump, but the renormalization after this jump is given by the system wave function, i.e., after determining the quantum jump time and the decay channel in the usual way [18] we replace $|\Phi(t)\rangle$ by

$$|\Phi(t^+)\rangle=e^{-iu\hat{z}}B_\sigma(z)|\Phi(t^-)\rangle/\|e^{-iu\hat{z}}B_\sigma(\hat{z})|\Phi(t^-)\rangle\| \quad \text{(A8)}$$

and $|\Psi(t)\rangle$ by

$$|\Psi(t^+)\rangle=e^{-iu\hat{z}}B_\sigma(\hat{z})|\Psi(t^-)\rangle/\|e^{-iu\hat{z}}B_\sigma(\hat{z})|\Phi(t^-)\rangle\|. \quad \text{(A9)}$$

An ensemble average over all possible (or in practice sufficiently many) trajectories gives

$$\rho_1(t)=\langle\langle(|\Phi(t)\rangle\langle\Psi(t)|+|\Psi(t)\rangle\langle\Phi(t)|)/\|\Phi(t)\|^2\rangle\rangle. \quad \text{(A10)}$$

A convenient choice for the function f in (A1) is $f(t)=\Delta(t-t_0)$ since we are directly interested in the momentum correlation function [cf. (A1)]. In this case the wave functions $|\Phi(t)\rangle$ and $|\Psi(t)\rangle$ are decoupled for times $t\neq t_0$ and the effect of $f(t)$ is to perturb the parasitic wavefunction $|\Psi(t)\rangle$ at time t_0 by applying the momentum operator $\hat{p}$ to it. This choice of $f(t)$ has therefore the convenient property that we can use the same propagation algorithm for both wave functions. Prior to t_0 these wave functions are identical, at t_0 the parasite is perturbed, and after t_0 the two wave functions evolve independently.

Finally, the momentum correlation function can now be simulated via

$$c_p(t;t_0)=\mathrm{tr}_s\hat{p}\rho_1(t)=\left\langle\!\!\left\langle\frac{\langle\Psi(t)|\hat{p}|\Phi(t)\rangle+\langle\Phi(t)|\hat{p}|\Psi(t)\rangle}{\|\Phi(t)\|^2}\right\rangle\!\!\right\rangle. \quad \text{(A11)}$$

We remark that even though it is possible to use the same approach as in Sec. II B, i.e., the method of localizing quantum jumps, in order to explicitly calculate the trajectories $|\Phi(t)\rangle$ it is computationally more efficient to perform these calculations with a periodic wave function. For more details on this see Ref. [7].

APPENDIX B: LONG-TIME LIMIT OF THE MOMENTUM CORRELATION FUNCTION

In this appendix we give the asymptotic expansion of the momentum correlation function of the Fokker-Planck equation (46) with the force (49) for large times. To achieve this we will use an eigenfunction method described in Ref. [13].

The Fokker-Planck equation considered here is of the form

$$\partial_t W(p,t) = -\partial_p[F(p)W(p,t)] + D\partial_p^2 W(p,t), \quad \text{(B1)}$$

with a force $F(p)$ that is antisymmetric in p and that decays as $-\alpha/p$ above a certain threshold p_a. We can assume $\alpha = p_a = 1$ since we can always use a scaling $\overline{p} = p/p_a$, $\overline{t} = t\alpha/p_a^2$ in order to achieve this with respect to the scaled variables. The scaled diffusion coefficient is then given by $\overline{D} = D/\alpha$. To be more precise, we assume the force to be

$$F(p) = \begin{cases} \widetilde{F}(p), & |p| < 1 \\ -1/p, & |p| > 1, \end{cases} \quad \text{(B2)}$$

where $\widetilde{F}(p)$ is some not explicitly specified but antisymmetric function of p. In the following we will denote a quantity in the region $|p| < 1$ with a tilde.

With the definition $\Phi(p) = f(p)/D$ where

$$f(p) = -\int_0^p d\zeta F(\zeta), \quad \text{(B3)}$$

we can write the stationary solution of (B1) as

$$W_{\mathrm{st}}(p) = Ne^{-\Phi(p)}, \quad \text{(B4)}$$

where N is a normalization constant. Using the explicit form (B2) we get

$$\Phi(p) = \begin{cases} \widetilde{\Phi}(p), & |p| < 1 \\ (1/D)\ln|p| + \widetilde{\Phi}(1), & |p| < 1. \end{cases} \quad \text{(B5)}$$

From this equation and (B4) we see that the stationary solution is proportional to $|p|^{-1/D}$ for $|p| > 1$, which necessitates $D < \frac{1}{3}$ in order to ensure the convergence of $\int dp\ p^2 W_{\mathrm{st}}(p)$. This is in order to guarantee the existence of the stationary momentum correlation function, which is defined by

$$c_p(t) \equiv \langle\langle p(t)p(0)\rangle\rangle_{\mathrm{st}} = \int dp\ pe^{\mathscr{L}t} pW_{\mathrm{st}}(p). \quad \text{(B6)}$$

Here, $\langle\langle\rangle\rangle_{\mathrm{st}}$ represents a stochastic average in stationary state and $e^{\mathscr{L}t}$ formally denotes the propagator for (B1).

We can get an explicit formula for this propagator in terms of eigenfunctions of the Fokker-Planck equation by transforming (B1) into an equivalent Schrödinger equation [13]. The eigenvalue problem then reads

$$H\psi_E(p) \equiv [-D\partial_p^2 + V_s(p)]\psi_E(p) = E\psi_E(p), \quad \text{(B7)}$$

which is equivalent to the eigenvalue problem for a particle with mass $M = (2D)^{-1}$ in the potential

$$V_s(p) = \frac{1}{4D}F^2(p) + \frac{1}{2}F'(p). \quad \text{(B8)}$$

Throughout this section a prime denotes differentiation with respect to p. In our case we get

$$V_s(p) = \begin{cases} \widetilde{V}_s(p), & |p| < 1 \\ \gamma/p^2, & |p| > 1, \end{cases} \quad \text{(B9)}$$

where $\gamma = 1/4D + 1/2$. The potential (B9) is symmetric due to the antisymmetry of the force and therefore the eigenfunctions can be chosen to be real and to have a certain parity. These eigenfunctions form a continuum with energies $E \geqslant 0$ since the potential goes to zero as $p \to \infty$. We will thus use the notation $\psi_E(p) \equiv \psi_k(p)$ for the antisymmetric and $\varphi_k(p)$ for the symmetric eigenfunctions with wave vectors $k \geqslant 0$.

The explicit form of the odd eigenfunctions—we will only need those later—is

$$\psi_k(p) = c\begin{cases} \widetilde{\psi}_k(p), & |p| < 1 \\ \sqrt{p}[c_1 J_\rho(kp) + c_2 Y_\rho(kp)], & |p| > 1, \end{cases} \quad \text{(B10)}$$

where J_ρ and Y_ρ denote the Bessel functions of the first and second kind of order $\rho = \sqrt{1/4 + \gamma/D}$, and $\widetilde{\psi}_k(p)$ is the odd (and real) solution to (B7) in the region $|p| < 1$, which we make unique by demanding $\lim_{p\to 1}\widetilde{\psi}_k(p) = 1$. The normalization constant c will later be calculated explicitly. The corresponding eigenvalues are $E_k = Dk^2$. The functions $c_{1,2}$ can be calculated by matching the eigenfunctions and their derivatives at $p = 1$. We get

$$c_1(k) = -\frac{\pi}{2}\{[v(k) - \tfrac{1}{2}]Y_\rho(k) - kY'_\rho(k)\},$$

$$c_2(k) = \frac{\pi}{2}\{[v(k) - \tfrac{1}{2}]J_\rho(k) - kJ'_\rho(k)\}, \quad \text{(B11)}$$

where we defined $v(k) = \widetilde{\psi}'_k(1) = v_0 + v_1 k + O(k^2)$.

The propagator for the Fokker-Planck equation can now be related to the propagator for the equivalent Schrödinger problem $i\partial_t \Psi = H\Psi$ with imaginary time via

$$e^{\mathscr{L}t} = e^{-\Phi/2}e^{-Ht}e^{\Phi/2}. \quad \text{(B12)}$$

Using this in conjunction with the completeness relation

$$\int_0^\infty dk\psi_k(p)\psi_k(\overline{p}) + \int_0^\infty dk\varphi_k(p)\varphi_k(\overline{p}) = \Delta(p - \overline{p}), \quad \text{(B13)}$$

we can write the correlation function as

$$c_p(t) = N\int_0^\infty dk\ G(k)^2 e^{-E_k t} \quad \text{(B14)}$$

with

$$G(k) = \int dp\,\psi_k(p)pe^{-\Phi(p)/2}. \quad \text{(B15)}$$

Note that (B15) only involves the odd eigenfunctions $\psi_k(p)$, which is due to the fact that $pW_{\mathrm{st}}(p)$ is an odd function itself. Since we are interested in the long-time behavior of (B14) it is only necessary to know the function $G(k)$ in the vicinity of $k = 0$. In order to find this behavior we expand $c_{1,2}(k)$ in powers of k:

$$c_1(k)=\frac{\Gamma(\rho)}{2}\left(\frac{2}{k}\right)^{\rho}[\rho-\tfrac{1}{2}+v_0+O(k)],$$

$$c_2(k)=\frac{\pi}{2\Gamma(\rho+1)}\left(\frac{k}{2}\right)^{\rho}[-\rho-\tfrac{1}{2}+v_0+O(k)]. \quad \text{(B16)}$$

The eigenfunctions (B10) are necessarily orthogonal, but have yet to be normalized. The normalization constant c is given by

$$c=\left(\frac{k/2}{c_1^2+c_2^2}\right)^{1/2}=\frac{2}{\Gamma(\rho)}\left(\frac{k}{2}\right)^{\rho+1/2}\left(\frac{1}{\rho-1/2+v_0}+O(k)\right), \quad \text{(B17)}$$

which guarantees the correct behavior $\psi_k(p)\underset{p\to\infty}{\to}\pi^{-1/2}\sin(kp-\phi_k)$ with some phase ϕ_k. The function $G(k)$ can now be evaluated to give

$$G(k)=c\int_{-1}^{1}dp\,\tilde{\psi}_k(p)pe^{-\tilde{\Phi}(p)/2}+2c\int_1^{\infty}dp\sqrt{p}\,[c_1J_\rho(kp)+c_2Y_\rho(kp)]p\frac{e^{-\tilde{\Phi}(1)/2}}{p^{1/2D}}. \quad \text{(B18)}$$

The first integral converges to a finite value as $k\to 0$ and can be neglected in comparison with the second one (see below), which can be written as

$$2ce^{-\tilde{\Phi}(1)/2}\left[c_1\int_1^{\infty}dp\;p^{-\mu}J_\rho(kp)+c_2\int_1^{\infty}dpp^{-\mu}Y_\rho(kp)\right], \quad \text{(B19)}$$

where we defined $\mu=1/2D-3/2=\rho-2$. The asymptotic behavior of the first integral can be found via the transformation $y=kp$:

$$I(k)=\int_1^{\infty}dp\;p^{-\mu}J_\rho(kp)=k^{\mu-1}\int_k^{\infty}dy\;y^{-\mu}J_\rho(y). \quad \text{(B20)}$$

The integral on the right-hand side exists in the limit $k\to 0$ and converges to $2^{-\mu-1}\sqrt{\pi}/\Gamma(\rho-1/2)$ and therefore

$$I(k)\sim\frac{\sqrt{\pi}}{2^{\mu+1}\Gamma(\rho-1/2)}k^{\mu-1}. \quad \text{(B21)}$$

Using this in conjunction with (B16) gives the asymptotic behavior

$$c_1(k)I(k)\sim\sqrt{\pi}(\rho-1/2+v_0)\frac{\Gamma(\rho)}{\Gamma(\rho-1/2)}k^{-3}. \quad \text{(B22)}$$

The asymptotic behavior of the second integral in (B19)

$$\mathbb{I}(k)=\int_1^{\infty}dpp^{-\mu}Y_\rho(kp)=k^{\mu-1}\int_k^{\infty}dyy^{-\mu}Y_\rho(y) \quad \text{(B23)}$$

can be calculated in a similar way to give

$$c_2(k)\mathbb{I}(k)\sim\begin{cases}\dfrac{\sqrt{\pi}\sin[(\mu+1)\pi]\Gamma(\mu-1/2)[\rho+1/2+v_0]}{2^{2\rho}\Gamma(\rho+1)}k^{2\rho-3}, & \rho<\frac{3}{2}\\ \dfrac{v_0-\rho-1/2}{2\rho(3-2\rho)}, & \rho>\frac{3}{2}.\end{cases} \quad \text{(B24)}$$

Therefore the asymptotic behavior of $G(k)$ is given by

$$G(k)\sim\frac{\sqrt{\pi}e^{-\tilde{\Phi}(1)/2}}{2^{\rho-3/2}\Gamma(\rho-1/2)}k^{\mu-1/2}, \quad \text{(B25)}$$

and therefore the asymptotic expansion of the momentum correlation function is given by

$$c_p(t)\sim\frac{W_{\mathrm{st}}(1)\pi(2\mu-3)^{\mu}}{4^{\mu+1}\mu(\mu+1)\Gamma(\mu+2)}t^{-\mu}. \quad \text{(B26)}$$

APPENDIX C: DISTRIBUTION OF EXIT POINTS FOR THE KRAMERS EQUATION

In this section we will give a derivation of the distribution of exit times following the method of Ref. [22]. We are considering the following Kramers equation:

$$\partial_t W(\overline{z,p,t})+\partial_{\overline{z}}\frac{\overline{p}}{M}W(\overline{z,p,t})=-\partial_{\overline{p}}\left(-\frac{\alpha}{\overline{p}}W(\overline{z,p,t})\right)+\overline{D}\partial_{\overline{p}}^2W(\overline{z,p,t}), \quad \text{(C1)}$$

where the force is inversely proportional to the momentum. Using the scaling

$$W(\overline{z,p,t})=w(\overline{z}\overline{M}/\sqrt{\alpha},\overline{p}/\sqrt{\alpha},t)=w(z,p,t) \quad \text{(C2)}$$

we get with the definition $D=\overline{D}/\alpha$:

$$\partial_t w(z,p,t)+\partial_z pw(z,p,t)=-\partial_p\left(-\frac{1}{p}w(z,p,t)\right)+D\partial_p^2w(z,p,t). \quad \text{(C3)}$$

In order to assure normalizability of the stationary solution, which goes as $p^{-1/D}$, we need $D>1$. We start with the particle prepared in a deterministic state (z_0,p_0) at time $t=0$ and look for the probability density $\pi_e(z,p,z_0,p_0)$ for exiting through the line $\{(z,p)|z\in(-\infty,\infty)\}$ (cf. Fig. 7). This will give us the distribution of distances the particle travels until its momentum falls below a certain threshold p. According to Ref. [22] the distribution function satisfies the equation

$$\frac{1}{p_0}\partial_{p_0}\pi_e(z,p,z_0,p_0)=p_0\partial_{z_0}\pi_e(z,p,z_0,p_0)+D\partial_{p_0}^2\pi_e(z,p,z_0,p_0), \quad \text{(C4)}$$

with the boundary condition

$$\pi_e(z,p,z_0,p_0=p)=\delta(z_0-z), \quad \text{(C5)}$$

$$\lim_{p_0\to\infty}\pi_e(z,p,z_0,p_0)=0. \quad \text{(C6)}$$

This problem can be solved using a separation ansatz. By using

$$\nu=\frac{1}{3D}+\frac{1}{3}>\frac{2}{3}, \quad \text{(C7)}$$

we can write the solution as

$$\pi_e(z,p,z_0,p_0)=\int_{-\infty}^{\infty}d\lambda\,\frac{e^{i\lambda(z_0-z)}}{2\pi}\,\frac{p_0^{3\nu/2}H_\nu^{(+)}(z_{p_0}(\lambda))}{p^{3\nu/2}H_\nu^{(+)}(z_p(\lambda))}, \quad \text{(C8)}$$

where $H_\nu^{(+)}(z)$ is the Hankel function with the asymptotic behavior $\lim_{z\to\infty}H_\nu^{(+)}(z)=\sqrt{2/(\pi z)}e^{i(z-\nu\pi/2-\pi/4)}$, and $z_\zeta(\lambda)=2\sqrt{|\lambda|/D}\zeta^{3/2}e^{i[\arg(\lambda)/2+\pi/4]}/3$ are V-shaped paths in the upper complex plane.

Using the series expansion for the Hankel functions

$$H_\nu^{(+)}(z)=J_\nu(z)+iY_\nu(z)=\frac{i}{\sin(\nu\pi)}\left(\frac{2}{z}\right)^\nu\left[\sum_{k=0}^{\infty}\frac{(-1)^{k+1}}{k!\Gamma(k-\nu+1)}\left(\frac{z}{2}\right)^{2k}+\left(\frac{z}{2i}\right)^{2\nu}\sum_{k=0}^{\infty}\frac{(-1)^k}{k!\Gamma(k+\nu+1)}\left(\frac{z}{2}\right)^{2k}\right], \quad \text{(C9)}$$

it is easy to show that the function $f(\lambda)=H_\nu^{(+)}(z_{p_0}(\lambda))/H_\nu^{(+)}(z_p(\lambda))$ has a series expansion

$$f(\lambda)=s_1(\lambda)+\lambda^\nu s_2(\lambda)+\lambda^{2\nu}s_3(\lambda)+\ldots, \quad \text{(C10)}$$

with analytical functions $s_n(\lambda)$ whose convergence radius is equal to the distance of the origin to the closest zero of $H_\nu^{(+)}(z_p(\lambda))$. We therefore find for $n\nu\neq 1,2,3,\ldots$ a branch cut of the $\lambda^{n\nu}$ function, and the corresponding discontinuity of a sufficiently large derivative of $f(\lambda)$. When taking the Fourier transform of $f(\lambda)$ according to Eq. (C8) these discontinuities produce slowly decaying parts of which the $n=1$ term is the dominant one. Using

$$\lim_{a\to 0_+}\int_{-\infty}^{\infty}d\lambda\;\lambda^\nu e^{-a|\lambda|}e^{-iz\lambda}=\begin{cases}\dfrac{\Gamma(\nu+1)}{z^{\nu+1}}[e^{-i(\nu+1)\pi/2}+e^{i(3\nu+1)\pi/2}], & z>0\\ 0, & z<0,\end{cases}$$

we get for $z\to\infty$ the asymptotic expansion

$$\pi_e(z,p,z_0,p_0)\sim\frac{1}{3^{2\nu}}\,\frac{(3\nu+1)^\nu}{\Gamma(\nu)}\,\frac{p_0^{3\nu}-p^{3\nu}}{(z-z_0)^{\nu+1}}. \quad \text{(C11)}$$

APPENDIX D: FIRST AND SECOND MOMENTS OF THE DISTRIBUTION OF FLIGHT TIMES FOR THE KRAMERS EQUATION

In this section we will calculate the first and second moments for the flight times of the above-barrier flights discussed in the previous Appendix.

The starting point is again the Fokker-Planck equation (B1) with the force (B2). Denoting the operator that acts on the right-hand side of Eq. (B1) on $W(p,t)$ with $\mathscr{L}(p)$, we can calculate the first two moments of the distribution of flight times (or mathematically the moments of the first return time) from the hierarchy of equations [13]:

$$\mathscr{L}(\tilde{p})w_1(\tilde{p},p_0)=-\delta(\tilde{p}-p_0),$$

$$\mathscr{L}(\tilde{p})w_2(\tilde{p},p_0)=-2w_1(\tilde{p},p_0). \quad \text{(D1)}$$

The boundary condition for the functions $w_{1,2}$ are

$$w_{1,2}(\tilde{p}=p,p_0)=0,\quad \lim_{\tilde{p}\to\infty}w_{1,2}(\tilde{p},p_0)=0. \quad \text{(D2)}$$

The first and second moments of the distribution of flight times when departing from p_0 and arriving at p (see Fig. 7), $T_1(p_0)$ and $T_2(p_0)$, can then be calculated via

$$T_n(p_0)=\int_p^\infty d\tilde{p}\,w_n(\tilde{p},p_0). \quad \text{(D3)}$$

Using the explicit form of the Fokker-Planck equation (B1) and the definition (C7) we can write the solution for the first equation in (D1) as

$$w_1(\tilde{p},p_0)=\frac{\tilde{p}}{1+D}\begin{cases}(1-p^{3\nu}\tilde{p}^{-3\nu}), & \tilde{p}<p_0\\ (p_0^{3\nu}-p^{3\nu})\tilde{p}^{-3\nu}, & \tilde{p}>p_0.\end{cases} \quad \text{(D4)}$$

From the behavior of this solution for large $\tilde{p}$ it is easy to see that the first momentum $T_1(p_0)$ exists for $\nu>\frac{2}{3}$.

The function $w_1(\tilde{p},p_0)$ enters the equation for $w_2(\tilde{p},p_0)$ as an inhomogeneity and it is straightforward to check that the large $\tilde{p}$ behavior of $w_2(\tilde{p},p_0)$ is therefore proportional to $p^{\sim -3(\nu-1)}$. Thus, the second moment $T_2(p_0)$ exists if $\nu>\frac{4}{3}$.

APPENDIX E: TWO-DIMENSIONAL OPTICAL LATTICES

After transforming the master equation (59) into the Wigner picture, and subsequent expansion in orders of $\hbar\boldsymbol{k}$ (up to second order), we get a bipotential equation for the two components of the Wigner operator

$$\left[\frac{\partial}{\partial t}+\frac{\boldsymbol{p}}{M}\cdot\boldsymbol{\nabla}_{\boldsymbol{x}}\right]f_{\pm}(\boldsymbol{x},\boldsymbol{p},t)=\langle\pm|\mathscr{L}^{(0)}W_{gg}(\boldsymbol{x},\boldsymbol{p},t)|\pm\rangle+\langle\pm|\mathscr{L}^{(1)}W_{gg}(\boldsymbol{x},\boldsymbol{p},t)|\pm\rangle+\langle\pm|\mathscr{L}^{(2)}W_{gg}(\boldsymbol{x},\boldsymbol{p},t)|\pm\rangle. \quad \text{(E1)}$$

This appendix summarizes the terms on the right-hand side of Eq. (E1) for electric fields of the form (62).

The zeroth-order term determines the transition rates between the optical potentials and can be written in the form

$$\langle\pm|\mathscr{L}^{(0)}W_{gg}(\boldsymbol{x},\boldsymbol{p},t)|\pm\rangle=\mp\tfrac{4}{9}\gamma_0\{|C(\boldsymbol{x})|^2f_+(\boldsymbol{x},\boldsymbol{p},t)-|S(\boldsymbol{x})|^2f_-(\boldsymbol{x},\boldsymbol{p},t)\}. \quad \text{(E2)}$$

The mechanical light force corresponds to the first-order term in the $\hbar\boldsymbol{k}$ expansion:

$$\begin{aligned}\langle\pm|\mathscr{L}^{(1)}W_{gg}(\boldsymbol{x},\boldsymbol{p},t)|\pm\rangle=&-\frac{1}{3}U_0\boldsymbol{\nabla}_{\boldsymbol{x}}\begin{pmatrix}3|S(\boldsymbol{x})|^2+|C(\boldsymbol{x})|^2\\ 3|C(\boldsymbol{x})|^2+|S(\boldsymbol{x})|^2\end{pmatrix}\cdot\boldsymbol{\nabla}_{\boldsymbol{p}}f_{\pm}(\boldsymbol{x},\boldsymbol{p},t)+\gamma_0\begin{pmatrix}i\boldsymbol{\nabla}_{\boldsymbol{x}}S^*(\boldsymbol{x})S(\boldsymbol{x})-iS^*(\boldsymbol{x})\boldsymbol{\nabla}_{\boldsymbol{x}}S(\boldsymbol{x})\\ \frac{1}{9}[i\boldsymbol{\nabla}_{\boldsymbol{x}}S^*(\boldsymbol{x})S(\boldsymbol{x})-iS^*(\boldsymbol{x})\boldsymbol{\nabla}_{\boldsymbol{x}}S(\boldsymbol{x})]\end{pmatrix}\\ &\cdot\boldsymbol{\nabla}_{\boldsymbol{p}}f_{\pm}(\boldsymbol{x},\boldsymbol{p},t)+\gamma_0\begin{pmatrix}\frac{1}{9}[i\boldsymbol{\nabla}_{\boldsymbol{x}}C^*(\boldsymbol{x})C(\boldsymbol{x})-iC^*(\boldsymbol{x})2\boldsymbol{\nabla}_{\boldsymbol{x}}C(\boldsymbol{x})]\\ i\boldsymbol{\nabla}_{\boldsymbol{x}}C^*(\boldsymbol{x})C(\boldsymbol{x})-iC^*(\boldsymbol{x})\boldsymbol{\nabla}_{\boldsymbol{x}}C(\boldsymbol{x})\end{pmatrix}\boldsymbol{\nabla}_{\boldsymbol{p}}\cdot f_{\pm}(\boldsymbol{x},\boldsymbol{p},t)\\ &+\frac{2\gamma_0}{9}\begin{pmatrix}i\boldsymbol{\nabla}_{\boldsymbol{x}}S^*(\boldsymbol{x})S(\boldsymbol{x})-iS^*(\boldsymbol{x})\boldsymbol{\nabla}_{\boldsymbol{x}}S(\boldsymbol{x})\\ i\boldsymbol{\nabla}_{\boldsymbol{x}}C^*(\boldsymbol{x})C(\boldsymbol{x})-iC^*(\boldsymbol{x})\boldsymbol{\nabla}_{\boldsymbol{x}}C(\boldsymbol{x})\end{pmatrix}\boldsymbol{\nabla}_{\boldsymbol{p}}\cdot f_{\mp}(\boldsymbol{x},\boldsymbol{p},t).\end{aligned} \quad \text{(E3)}$$

The last of these terms in Eq. (E3) gives rise to a deterministic momentum change when the atom is optically pumped from one optical potential into the other. The intrawell and interwell ''diffusion'' (associated with a fuzzy jump between the optical potentials) is determined by the second-order term, which is not necessarily positive definite everywhere. These negativities are quantum features of the atomic center-of-mass motion. A thorough discussion of this point can be found in Ref. [17] (numerically we truncate this negative parts by setting the ''diffusion'' equal to zero in these negative regimes, thus ''slightly'' overestimating the heating to some extent):

$$\begin{aligned}\langle\pm|\mathscr{L}^{(2)}W_{gg}(\boldsymbol{x},\boldsymbol{p},t)|\pm\rangle=&\frac{\gamma_0}{6}\frac{\partial^2}{\partial x_i\partial x_j}\begin{pmatrix}3|S(\boldsymbol{x})|^2+|C(\boldsymbol{x})|^2\\ 3|C(\boldsymbol{x})|^2+|S(\boldsymbol{x})|^2\end{pmatrix}\frac{1}{2}\frac{\partial^2}{\partial p_i\partial p_j}f_{\pm}(\boldsymbol{x},\boldsymbol{p},t)+\gamma_0\frac{2}{9}\kappa^{ij}_{++}\begin{pmatrix}9|S(\boldsymbol{x})|^2\\ |S(\boldsymbol{x})|^2\end{pmatrix}\frac{1}{2}\frac{\partial^2}{\partial p_i\partial p_j}f_{\pm}(\boldsymbol{x},\boldsymbol{p},t)\\ &+\gamma_0\frac{2}{9}\kappa^{ij}_{--}\begin{pmatrix}|C(\boldsymbol{x})|^2\\ 9|C(\boldsymbol{x})|^2\end{pmatrix}\frac{1}{2}\frac{\partial^2}{\partial p_i\partial p_j}f_{\pm}(\boldsymbol{x},\boldsymbol{p},t)+\gamma_0\frac{4}{9}\kappa^{ij}_{00}\begin{pmatrix}|S(\boldsymbol{x})|^2\\ |C(\boldsymbol{x})|^2\end{pmatrix}\frac{1}{2}\frac{\partial^2}{\partial p_i\partial p_j}f_{\mp}(\boldsymbol{x},\boldsymbol{p},t)\\ &+\gamma_0\frac{2}{3}\begin{pmatrix}\kappa^{ij}_{+-}S(\boldsymbol{x})C(\boldsymbol{x})^*+\text{c.c.}\\ \kappa^{ij}_{+-}S(\boldsymbol{x})C(\boldsymbol{x})^*+\text{c.c.}\end{pmatrix}\frac{1}{2}\frac{\partial^2}{\partial p_i\partial p_j}f_{\pm}(\boldsymbol{x},\boldsymbol{p},t)+\frac{\gamma_0}{2}\frac{1}{2}\frac{\partial^2}{\partial p_i\partial p_j}f_{\pm}(\boldsymbol{x},\boldsymbol{p},t)\\ &\times\left\{\begin{pmatrix}-\frac{\partial^2}{\partial x_i\partial x_j}[S^*(\boldsymbol{x})]S(\boldsymbol{x})-S^*(\boldsymbol{x})\frac{\partial^2}{\partial x_i\partial x_j}S(\boldsymbol{x})\\ -\frac{1}{9}\frac{\partial^2}{\partial x_i\partial x_j}[S^*(\boldsymbol{x})]S(\boldsymbol{x})-\frac{1}{9}S^*(\boldsymbol{x})\frac{\partial^2}{\partial x_i\partial x_j}S(\boldsymbol{x})\end{pmatrix}\right.\\ &\left.+\begin{pmatrix}\frac{\partial}{\partial x_i}[S^*(\boldsymbol{x})]\frac{\partial}{\partial x_j}S(\boldsymbol{x})\frac{\partial}{\partial x_j}[S^*(\boldsymbol{x})]\frac{\partial}{\partial x_i}S(\boldsymbol{x})\\ \frac{1}{9}\frac{\partial}{\partial x_i}[S^*(\boldsymbol{x})]\frac{\partial}{\partial x_j}S(\boldsymbol{x})\frac{1}{9}\frac{\partial}{\partial x_j}[S^*(\boldsymbol{x})]\frac{\partial}{\partial x_i}S(\boldsymbol{x})\end{pmatrix}\right\}+\frac{\gamma_0}{2}\frac{1}{2}\frac{\partial^2}{\partial p_i\partial p_j}f_{\pm}(\boldsymbol{x},\boldsymbol{p},t)\end{aligned}$$

$$\times\left\{\begin{pmatrix} -\frac{1}{9}\frac{\partial^2}{\partial x_i\partial x_j}[C^*(\boldsymbol{x})]C(\boldsymbol{x})-\frac{1}{9}C^*(\boldsymbol{x})\frac{\partial^2}{\partial x_i\partial x_j}C(\boldsymbol{x}) \\ -\frac{\partial^2}{\partial x_i\partial x_j}[C^*(\boldsymbol{x})]C(\boldsymbol{x})-C^*(\boldsymbol{x})\frac{\partial^2}{\partial x_i\partial x_j}C(\boldsymbol{x}) \end{pmatrix}\right.$$

$$\left.+\begin{pmatrix} \frac{1}{9}\frac{\partial}{\partial x_i}[C^*(\boldsymbol{x})]\frac{\partial}{\partial x_j}C(\boldsymbol{x})+\frac{1}{9}\frac{\partial}{\partial x_j}[C^*(\boldsymbol{x})]\frac{\partial}{\partial x_i}C(\boldsymbol{x}) \\ \frac{\partial}{\partial x_i}[C^*(\boldsymbol{x})]\frac{\partial}{\partial x_j}C(\boldsymbol{x})+\frac{\partial}{\partial x_j}[C^*(\boldsymbol{x})]\frac{\partial}{\partial x_i}C(\boldsymbol{x}) \end{pmatrix}\right\}+\frac{\gamma_0}{9}\frac{1}{2}\frac{\partial^2}{\partial p_i\partial p_j}f_{\mp}(\boldsymbol{x},\boldsymbol{p},t)$$

$$\times\left\{\begin{pmatrix} -\frac{\partial^2}{\partial x_i\partial x_j}[S^*(\boldsymbol{x})]S(\boldsymbol{x})-S^*(\boldsymbol{x})\frac{\partial^2}{\partial x_i\partial x_j}S(\boldsymbol{x}) \\ -\frac{\partial^2}{\partial x_i\partial x_j}[C^*(\boldsymbol{x})]C(\boldsymbol{x})-C^*(\boldsymbol{x})\frac{\partial^2}{\partial x_i\partial x_j}C(\boldsymbol{x}) \end{pmatrix}\right.$$

$$\left.+\begin{pmatrix} \frac{\partial}{\partial x_i}[S^*(\boldsymbol{x})]\frac{\partial}{\partial x_j}S(\boldsymbol{x})+\frac{\partial}{\partial x_j}[S^*(\boldsymbol{x})]\frac{\partial}{\partial x_i}S(\boldsymbol{x}) \\ \frac{\partial}{\partial x_i}[C^*(\boldsymbol{x})]\frac{\partial}{\partial x_j}C(\boldsymbol{x})+\frac{\partial}{\partial x_j}[C^*(\boldsymbol{x})]\frac{\partial}{\partial x_i}C(\boldsymbol{x}) \end{pmatrix}\right\}. \tag{E4}$$

The spatial variances of spontaneous photon emission κ_σ^{ij} are given by

$$\kappa_{\pm\pm}^{xx}=\kappa_{\pm}^{yy}=\frac{3k^2}{10},\quad \kappa_{00}^{xx}=\kappa_0^{yy}=\frac{4k^2}{10},$$

$$\kappa_{\sigma\sigma}^{xy}=0 \quad \text{for} \quad \sigma=0,\pm,$$

$$\kappa_{\pm\mp}^{xx}=\frac{k^2}{10},\quad \kappa_{\pm\mp}^{yy}=-\frac{k^2}{10},$$

$$\kappa_{+-}^{xy}=\kappa_{-+}^{xy}=-\frac{ik^2}{10}, \tag{E5}$$

respectively.

[1] H. Wallis, Phys. Rep. **255**, 203 (1995).

[2] C. Cohen-Tannoudji, in *Fundamental Systems in Quantum Optics*, Les Houches, Session LIII, edited by J. Dalibard, J. M. Raimond, and J. Zinn-Justin (Elsevier, Amsterdam, 1992).

[3] J. Dalibard and C. Cohen-Tannoudjii, J. Opt. Soc. Am. B **6**, 2023 (1989).

[4] Y. Castin and J. Dalibard, Europhys. Lett. **14**, 761 (1991).

[5] P. S. Jessen, C. Gertz, B. D. Lett, W. D. Phillips, S. L. Rolston, R. J. C. Spreeuw, and C. I. Westbrook, Phys. Rev. Lett. **69**, 49 (1992); P. Verkerk, B. Lounis, C. Salomon, C. Cohen-Tannoudji, J.-Y. Courtois, and G. Grynberg, Phys. Rev. Lett. **68**, 3861 (1992); P. Marte, R. Dum, R. Taieb, P. D. Lett, and P. Zoller, *ibid.* **71**, 1335 (1993).

[6] T. W. Hodapp, C. Gerz, C. Furthlehner, C. I. Westbrook, W. D. Phillips, and J. Dalibard, Appl. Phys. B **60**, 135 (1995).

[7] P. Marte, R. Dum, R. Taieb, and P. Zoller, Phys. Rev. A **47**, 1378 (1993).

[8] M. Holland, S. Marksteiner, P. Marte, and P. Zoller (unpublished).

[9] As will be shown in Sec. III ''sufficiently high'' means large enough to shift out of the regime of the strong Sisyphus force into the regime where the friction force decays as p^{-1}.

[10] J.-P. Bouchaud and A. Georges, Phys. Rep. **195**, 127 (1990).

[11] M. F. Shlesinger, G. M. Zaslavsky, and J. Klafter, Nature **363**, 31 (1993).

[12] F. Bardou, J. P. Bouchaud, O. Emile, A. Aspect, and C. Cohen-Tannoudji, Phys. Rev. Lett. **72**, 203 (1994).

[13] H. Risken, *The Fokker-Planck Equation* (Springer, Berlin, 1984).

[14] Y. Castin, J. Dalibard, and C. Cohen-Tannoudji, in *Proceedings of the LIKE Workshop*, edited by L. Moi *et al.* (ETS Editrice, Paris, 1991).

[15] G. Grynberg, B. Lounis, P. Verkerk, J.-Y. Courtois, and C. Salomon, Phys. Rev. Lett. **70**, 2249 (1993).

[16] A. Hemmerich and T. W. Hänsch, Phys. Rev. Lett. **70**, 410 (1993).

[17] Y. Castin, K. Berg-Sørensen, J. Dalibard, and K. Mølmer, Phys. Rev. A **50**, 5092 (1994).

[18] R. Dum, P. Zoller, and H. Ritsch, Phys. Rev. A **45**, 4879 (1992); C. W. Gardiner, A. S. Parkins, and P. Zoller, *ibid.* **46**, 4363 (1992); R. Dum, A. S. Parkins, P. Zoller, and C. W. Gardiner, *ibid.* **46**, 4382 (1992); J. Dalibard, Y. Castin, and K.

Mølmer, Phys. Rev. Lett. **68**, 580 (1992); K. Mølmer, Y. Castin, and J. Dalibard, J. Opt. Soc. Am. B **10**, 524 (1993); N. Gisin and I. C. Percival, Phys. Lett. A **167**, 315 (1992).

[19] For the coherent propagation of the atom in between spontaneous emissions we use a split-operator FFT algorithm [7], which turned out to be fast, reliable, and easy to implement. For the localizing quantum jump simulations and parameters used here a dynamical grid size of 8 wavelengths is sufficient to store the wave function during all of its random walk. Note that the size of the dynamic grid is determined by the average time between successive spontaneous emissions, since this gives the time in which the atomic wave function will spread out coherently.

[20] T. Bergeman, Phys. Rev. A **48**, R3425 (1993).

[21] J. P. Gordon and A. Ashkin, Phys. Rev. A **21**, 1606 (1980); S. Stenholm, Rev. Mod. Phys. **58**, 699 (1986); A. S. Parkins and P. Zoller, Phys. Rev. A **45**, 6522 (1992); G. Nienhuis, P. van der Straten, and S.-Q. Shang, *ibid.* **44**, 462 (1991).

[22] C. W. Gardiner, *Handbook of Stochastic Methods* (Springer, Berlin, 1983).

[23] R. N. Mantegna and H. E. Stanley, Phys. Rev. Lett. **73**, 2946 (1994).

[24] J. Guo, P. R. Berman, P. Dubetsky, and G. Grynberg, Phys. Rev. A **46**, 1426 (1992); J.-Y. Courtois, G. Grynberg, B. Lounis, and P. Verkerk, Phys. Rev. Lett. **72**, 3017 (1994).

[25] K. Berg-Sørensen, Phys. Rev. A **49**, R4297 (1994).